IN-SITU DEGASSING STUDIES ON CRYSTAL-FREE AND CRYSTAL-BEARING STROMBOLI BASALTS: IMPLICATIONS FOR STROMBOLI VOLCANO ERUPTIONS

Thesis

Liping Bai

Earth and Planetary Sciences

3450 University Street

McGill University, Montréal, Quebec, Canada H3A 2A7

March 12, 2012

A thesis submitted to McGill University in partial fulfillment of the requirements of the degree of Doctor of Science

ABSTRACT

Stromboli volcano (Aeolian Islands, Italy) has two types of magma: volatile-rich, aphyric magma (LP) that produces pumices and volatile-poor, highly porphyritic magma (HP) that produces scoria. This work studies how changes of magma properties affect the bubble formation and growth, and the dynamics of volcano eruptions. The first part of this work is a study of bubble formation and growth in crystal-free Stromboli basalts. Using X-ray microtomography (μCT) I studied the 3-D bubble sizes and distributions, determined the permeability with lattice-Boltzmann simulations and laboratory measurements, investigated the factors that control the occurrence of Darcian and non-Darcian flow, and delineated the Darcian and non-Darcian flow regimes in the vesicular Stromboli basalts by constraining the correlations between friction factor (f_k) and Forchheimer number (Fo). The second part of this work is based upon degassing experiments of crystal-bearing basalts at a synchrotron X-ray beamline. I studied 3-D crystal sizes and distributions, investigated the crystal effect on bubble sizes and distributions with X-ray μCT, and measured the magma permeability. The results demonstrate that the permeabilities of crystal-bearing Stromboli basalts are about 1 to 2 orders of magnitude higher than those in crystal-free samples in the porosity range of 31.6 to 55.3%.

Based on my experimental results, I propose that the higher permeability in crystal-bearing samples results in highly efficient degassing in the shallow, highly porphyritic (HP) magma as opposed to the deeper, aphyric (LP) magma. The LP magma flows up in a cylindrical conduit due to the density and viscosity difference between the two magmas. We calculated the ascending LP magma volume flux and the descending HP magma volume flux, showing that LP magma can be efficiently transferred through the overlying HP magma, implying that this type of convection can potentially cause the more-violent paroxysmal explosions occasionally observed at Stromboli.

RÉSUMÉ

Le volcan Stromboli (îles Éoliennes, Italie) a deux types de magma: un magma aphyrique, riche en volatiles et produisant du pumice, et un magma hautement porphyritique produisant de la scorie. Cette étude documente l'influence de variations en propriétés magmatiques sur la formation et la croissance de bulles, et leur impact sur la dynamique des éruptions volcaniques. En première partie, la formation et la croissance des bulles a été étudiée dans les basaltes stromboliens sans cristaux. J'ai étudié par microtomographie en rayons-X la distribution tri-dimensionnelle et la taille des bulles dans ces basaltes vésiculés, quantifié leur perméabilité par des simulations de type Boltzmann sur réseau et par des mesures en laboratoire, investigué les facteurs qui contrôlent l'écoulement darcien et non-darcien, et délimité ces deux régimes en contraignant les corrélations entre le facteur de friction (f_k) et le nombre Forchheimer (Fo). La deuxième partie est une étude expérimentale in situ sur une ligne synchrotron du dégazage de basaltes contenant des cristaux. La distribution tri-dimensionnelle des cristaux et leur effet sur la taille des bulles et la perméabilité du magma ont été quantifiés par microtomographie rayons-X. Les valeurs de perméabilité des basaltes de Stromboli contenant des cristaux sont d'un à deux ordres de grandeur plus élevées que celles de basaltes sans cristaux, pour des valeurs de perméabilité allant de 31.6 à 55.3%.

Ces résultats expérimentaux suggèrent que la perméabilité plus élevée des échantillons de basaltes contenant des cristaux favorise le dégazage des magmas hautement porphyritiques situés à faible profondeur, relatif aux magmas aphyriques et présents à plus grande profondeur. Le magma aphyrique remonte le long d'un conduit cylindrique à cause des différences de densité et viscosité entre les deux types de magmas. Des calculs de flux volumique d'un magma aphyrique ascendant et d'un magma porphyritique descendant démontrent que le magma aphyrique peut circuler efficacement et traverser un magma porphyritique sus-jacent. Ce type de convection pourrait potentiellement causer les éruptions paroxysmales observées sporadiquement à Stromboli.

TABLE OF CONTENTS

ABSTRACT II

RÉSUMÉ III

LIST OF FIGURES VI

LIST OF TABLES VIII

ACKNOWLEDGEMENTS IX

PREFACE X

CHAPTER 1: GENERAL INTRODUCTION 1

CHAPTER 2: CRYSTALLIZATION EXPERIMENTS, DEGASSING EXPERIMENTS AND PERMEABILITY STUDY METHODS 10

2.1 DEGASSING EXPERIMENTS ON CRYSTAL-FREE SAMPLES 10

2.2 CRYSTALLIZATION AND DEGASSING EXPERIMENTS ON CRYSTAL-BEARING SAMPLES 12

2.3 PERMEABILITY STUDY METHODS 13

2.3.1 Defining permeability in porous media 13

2.3.2 Lattice-Boltzmann simulations 15

2.3.3 Permeability measurement techniques 17

CHAPTER 3: INVESTIGATING THE EFFECTS OF SAMPLE SIZE AND RESOLULTION ON POROSITY AND PERMEABILITY 19

3.1 SAMPLE SIZE EFFECTS ON PERMEABILITY FROM LATTICE-BOLTZMANN SIMULATIONS 19

3.2 RESOLUTION EFFECTS ON POROSITY AND CALCULATED PERMEABILITY 20

CHAPTER 4: PERMEABILITY RESULS FROM MEASUREMENTS AND LATTICE-BOLTZMANN SIMULATIONS 27

4.1 DARCIAN PERMEABILITY OF CRYSTAL-FREE SAMPLES FROM LATTICE-BOLTZMANN SIMULATION AND MEASUREMENTS 27

4.1.1 Permeability-porosity relations 27

4.1.2 Forchheimer permeability constants k_1 and k_2 29

4.2 CRYSTAL AND BUBBLE SIZE DISTRIBUTION, BUBBLE NUMBER DENSITY, AND PERMEABILITY IN CRYSTAL-BEARING SAMPLES 31

4.2.1 Crystal sizes and distributions 31

4.2.2 Bubble number density, bubble shape, size, distribution, and permeability 32

CHAPTER 5: DISCUSSION 46

5.1 COMPARISON LATTICE-BOLTZMANN PERMEABILITIES WITH OTHER STUDIES 46

5.2 COMPARISON BETWEEN SIMULATED AND MEASURED PERMEABILITIES OF CRYSTAL-FREE EXPERIMENTS WITH VOLCANIC ROCKS 46

5.3 BUBBLE SIZE AND DISTRIBUTION EFFECTS ON k_1 AND k_2 IN CRYSTAL-FREE EXPERIMENTS 48

5.4 CORRELATION BETWEEN FRICTION FACTOR f_k AND FORCHHEIMER NUMBER *Fo* IN CRYSTAL-FREE EXPERIMENTS 51

5.5 THE EFFECT OF CRYSTALS ON BUBBLE GROWTH, BUBBLE SIZE AND DISTRIBUTION 54

5.6 PERMEABILITY COMPARISON BETWEEN CRYSTAL-FREE, CRYSTAL BEARING SAMPLES AND NATURAL SCORIA 56

CHAPTER 6: IMPLICATIONS FOR STOMBOLI BASALT VOLCANO 64

6.1 IMPLICATIONS FOR DARCIAN TO NON-DARCIAN FLOW TRANSITIONS 64

6.2 IMPLICATIONS FOR MAGMA CONVECTION IN STROMBOLI VOLCANO CONDUIT 66

CHAPTER 7: CONCLUSIONS 70

REFERENCES 73

LIST OF FIGURES

Figure 1.1 Map of Stromboli island ……..……..……....7
Figure 3.1 Dimensionless velocity from a lattice-Boltzmann simulation of flow in sample St25a with a porosity of 87.4%…….……..……...…..22
Figure 3.2 Calculated permeabilities for the samples, but with different simulation sizes (**a**) and with different grid sizes produced from the coarsening process (**b**)…….....23
Figure 3.3 3-D cumulative (open circles) and non-cumulative (bars) bubble size distributions of sample Bt1b imaged at high resolution (black symbol) and low resolution (green symbol))….……..……..…….……..……...24
Figure 4.1 Permeability k and total porosity ϕ relationships from lattice-Boltzmann simulations and measurements (**a**) and permeability and porosity of relationships at porosities above 29%, the percolation threshold (**b**)……..…..…..34
Figure 4.2 Scanning electron microscope images of samples St66b with a porosity of 46.3% (**a**) and St58a with a porosity of 66.7% (**b**) ……..……..35
Figure 4.3 a: Experimental data of $\frac{P_i^2 - P_o^2}{2PL}$ vs u_g for selected samples; **b**: Experim-
-ental data of $\frac{P_i^2 - P_o^2}{2PLu_g^2}$ vs u_g for selected samples …….…..…..…..36
Figure 4.4 a: Relationships between Darcian permeability k_1 and non-Darcian permeability k_2; **b**: Correlation between Darcian permeability k_1 and bubble diameter D (μm); **c**: Correlation between non-Darcian permeability k_2 and bubble diameter D (μm)…….……..……..…….....37
Figure 4.5 Backscattered electron images of crystal- and bubble-bearing samples Bt1a(**a**), SC23a(**b**), Bt7R(**c**), and Bt27(**d**)….……..……..……...…...38
Figure 4.6 3-D cumulative (open circles) and non-cumulative (bars) crystal size distributions from tomographic images of experimental crystal-bearing Stromboli basalt samples Bt7R(**a**) and SC23a(**b**), and natural scoria from Stromboli Str240506b_b3(**c**) and Str250506_c2(**d**)..…….……..……..…….....39
Figure 4.7 2-D slices from 3-D X-ray microtomography of the degassed crystal-bearing samples Bt1b(**a**), Bt7c(**b**), SC23c(**c**), Bt22a(**d**)….……..……..…..…40
Figure 4.8 3-D cumulative (open circles) and non-cumulative (bars) bubble size distributions in experimentally produced, crystal-bearing, degassed Stromboli basalt samples Bt1c(**a**) and SC23c(**b**), and natural Stromboli scoria Str240506 b_b3 (**c**) and Str250506_c2(**d**)….……..……..……..……...41
Figure 5.1 3-D bubble size distributions from 3-D tomographic images of experim-
-entally produced vesicular Stromboli basalt samples with different porosities.....59
Figure 5.2 Permeability constants k_1 and k_2 and porosity-pore size relationships from measurements (**a, b**), and the relation between the geometry factor of α and the bubble diameter D (μm) (**c**)…….……..……..…61
Figure 5.3 Relationship between the friction factor, f_k, and the Forchheimer number, Fo, for experimental measurements (**a**) and for lattice-Boltzmann simulations (**b**) from samples with different porosities …….……..…...…62

Figure 5.4 Permeability, *k*, and total porosity, ϕ, relationships from lattice-Boltzmann simulations and measurements in crystal-bearing samples ….……..…….……63
Figure 6.1 Relationship between volume fraction of H_2O and pressure (**a**) and permeability and depth (**b**)…….……..…….…..…...69

LIST OF TABLES

Table 1.1 Notation and description of the notation ……..……..……..8
Table 2.1 Crystallization experiments and results…….……..……...18
Table 3.1 Simulation results from coarsening samples …….…..….25
Table 3.2 Permeability simulation results from samples imaged with different voxel sizes……..…….…….26
Table 4.1 Description of crystal-free samples and permeability results ……...42
Table 4.2 Description of crystal-bearing samples and permeability results from degassing experiments …….44

ACKNOWLEDGEMENTS

Many people need to be thanked for their valuable contributions to this work. First, I thank my supervisor, Prof. Don R. Baker, who lead me into the field of synchrotron X-ray microtomography and volcanology. His enthusiasm and kindness allowed me to meet many experts in this field. Also, his critical questions and thinking made me continually improve myself in my studying and working at McGill. I appreciate Prof. Reghan J. Hill for his suggestions and guidance in my projects. I profited a lot from his deep knowledge of fluid dynamics and great ideas for my projects and papers. I thank Dr. Margherita Polacci for guiding me to study natural samples. Her great experiences and ideas in volcanology broadened my views in the field.

Prof. Don R. Baker, Prof. Reghan J. Hill and Dr. Margherita Polacci gave me the guidance throughout my Ph.D. study. I also thank the other members of my graduate committee: Don Francis, William Minarik, and Olivia Jensen; their critical questions pushed me to study a lot during my studying.

I also thank Cedrick O'Shaughnessy, Alexandra Larue, and Viktoria Maneta for their help during my experiments and study at McGill. They helped me prepared some samples and gave me some advice on the experiments. To work with them together in our geochemistry lab was a wonderful experience for me.

I especially thank Anne Kosowski, Kristy Thornton, and Angela Di Ninno for their help in my studying and immigration file preparations.

I also thank Mark Rivers and Lucia Mancini for their help in my X-ray microtomography work at APS and SLS. Mark Rivers helped us set up the X-ray microtomography experimental equipments, taught us how to perform X-ray microtomography. Lucia Mancini helped us perform the X-ray microtomography analysis and collect some data at SLS. I enjoyed and appreciated working with them in the synchrotron X-ray microtomography.

PREFACE

All of these results in this thesis were originally written as manuscripts, which were published in the Journal of Geophysical Research (JGR) and Geophysical Research Letters (GRL). The paper in JGR was co-authored with D R Baker and R J Hill, and paper in GRL was co-authored with D R Baker, M Polacci and R J Hill. I was the first author of both papers, and I was the main contributor to these works. My coauthors helped to perform experiments, assist with LB simulations, and to edit my manuscripts by giving advice and through discussions.

CHAPTER 1: GENERAL INTRODUCTION

Magma degassing consists of two fundamental processes, bubble nucleation and bubble growth. Two kinds of bubble nucleation mechanisms exist: homogeneous nucleation and heterogeneous nucleation. According to classical nucleation theory, bubble nucleation is initiated by the formation of critical-size nuclei (Sparks, 1978; Navon and Lyakhovsky, 1998; Frank et al., 2007). Homogeneous nucleation occurs in the pure and homogenous melt. Heterogeneous nucleation occurs when the heterogeneities such as crystals are present because the surface energy of the crystal-gas interface is lower than that of melt-gas interface (Hurwitz and Navon, 1994; Navon and Lyakhovsky, 1998). Previous degassing studies were primarily concerned with bubble nucleation and growth in silicic melts without the presence of crystals (Hurwitz and Navon, 1994; Gardner et al., 1999; Larsen and Gardner, 2000; Martel and Bureau, 2001; Larsen et al., 2004; Bai et al., 2008). These degassing experiments provide fundamental information on the bubble number density, the bubble growth rate, the bubble size distribution, and the vesicularity in the crystal-free magma. However, during magma degassing, magmas are usually not crystal free. The crystals may play an important role in the magma vesiculation process because crystals can have a profound effect on the kinetics of bubble nucleation, affect the degree of supersaturation required for bubble nucleation, and influence bubble size and bubble number density (Hurwitz and Navon, 1994; Mangan et al., 2004; Gardner, 2007; Cluzel et al., 2008; Belien et al., 2010). This study investigated degassing on both crystal-free and crystal-bearing Stromboli basaltic melts.

Stromboli volcano, located in the southern Tyrrhenian Sea in the Aeolian Archipelago, Italy (Figure 1.1), has a volcanic cone that rises 924 m above the sea level (Rosi et al., 2006; Martino et al., 2011). Stromboli has been almost continuously active since at least Roman times and has been called the “light house of the Mediterranean” (Barberi et al., 1993). It is an excellent natural laboratory for the investigation of volcanic processes and is intensively monitored and studied by many research groups.

Stromboli is characterized by oscillation between high frequency, low-volume, low-intensity, Strombolian eruptions and larger volume, low-frequency, high-intensity paroxysmal explosions (Barberi et al., 1993; Ripepe and Harris, 2008). Stromboli also exhibits lava effusion events that can last from days to months (Landi et al., 2006; Métrich et al., 2010).

Stromboli produces two types of ejecta that reflect two types of magmas at depth and different eruption styles; they have similar basaltic compositions but differ in crystal and vesicle content (Métrich et al., 2005). The common pattern of Stromboli is an almost-continuous sequence of mild explosions that are episodically punctuated by paroxysmal explosions. During normal eruptions and lava flow effusions, Stromboli basalts are characterized by low to moderate vesicularity, averaging 47%, and are crystal-rich (~ 50 vol.%) scoriaceous magma (Bertaginini et al., 1999; Francalanci et al., 2004; Polacci et al., 2009; Métrich et al., 2010). Scoria clasts from normal Strombolian activity have high density and contain abundant millimeter-size, spherical to sub-spherical vesicles, as well as large, sub-spherical to slightly deformed, interconnected vesicles. Paroxysmal explosions generally produce volatile-rich, highly vesicular (~ 70 to 75%), crystal-poor (less than 5 to 10 vol.%) pumice derived from a deep, volatile-rich magma (Métrich et al., 2005). Melt inclusions in olivine crystals indicate that the major volatile concentration in the crystal-poor magma are H_2O (~ 1.8 to 3.4 wt%), CO_2 (~ 707 to 1887 ppm), S (1660 to 2250 ppm), and Cl (1660 to 2030 ppm) (Métrich et al., 2001; Bertaginini et al., 2003). Vesicles in pumice are characterized by small to intermediate, mm-sized, tube-shaped vesicles with few larger ellipsoidal vesicles (Polacci et al., 2006).

Normal strombolian activity is believed to be driven by gas slugs bursting intermittently at the vent (Vergniolle et al., 1996). Lava effusions at Stromboli are initiated by a gradual pressure increase in the magma conduit that drives the shallow, volatile-poor magma upward (Landi et al., 2006). The proposed mechanisms of paroxysmal explosions include: the ascent of gas-rich magma that induces an increase of magmatic pressure (Ripepe and Harris, 2008); decreased degassing efficiency of the deeper system (Polacci et al., 2009); accumulation and disruption of CO_2-rich foams that

grow at interfaces within the magma chamber at depths on the order of a few kilometers, where gas-rich aphyric magma interacts with volatile-poor, crystal-rich magma (Allard, 2010); and the depressurization of the deep plumbing system due to lava effusion that induces voluminous degassing and eventually destabilizes the crystal-poor magma (Aiuppa et al., 2010).

The permeability of vesicular magma plays a vital role in controlling magmatic degassing in volcanic conduits. Permeabilities of magma affect the degassing efficiency because permeability controls gas loss during volcanic eruptions (e.g., Jaupart and Vergniolle, 1989; Klug and Cashman, 1996). Degassing experiments on vesicular material analogous to that involved in volcanic conduit magma flow (Vergniolle and Jaupart, 1990; Seyfried and Freundt, 2000) and numerical modelling studies of 1-D and 2-D flow (Jaupart and Allegre, 1991; Melnik and Sparks, 1999; Collombet, 2009) indicate that efficient gas loss occurs when the ascending magma becomes permeable with interconnected bubbles providing pathways for rapid gas escape. This is consistent with the generally accepted permeable degassing model of volcanic eruptions (e.g., Eichelberger et al., 1986; Aiuppa et al., 2007). Observations of pumice and scoria (Klug and Cashman, 1996; Marti et al., 1999; Klug et al., 2002; Wright et al., 2006) and degassing experiments on vesicular rhyolite or basalt (Eichelberger et al., 1986; Burgisser and Gardner, 2005; Bai et al., 2008) indicate that bubbles can form networks when their abundance exceeds a critical porosity. The development of a permeable bubble network is determined by bubble growth and coalescence, bubble aperture size, and shearing (Klug and Cashman, 1996; Saar and Manga, 1999; Wright et al., 2009). Following percolation theory, a connected network of random, equal-sized spherical pores in a vesicular material occurs at a threshold value (~ 29 volume percent), and the transport properties of vesicular material, including permeability and conductivity, are expected to show a significant variation either at this percolation threshold value or at another critical porosity (Rintoul and Torquato, 1997). Synthetic models of vesicle geometries indicate that the percolation threshold is affected by the bubble shape, bubble size distribution, and deformation (Blower, 2001). Although most studies found abrupt increases in permeability at porosities near 30% (Saar and Manga, 1999; Rust and Cashman, 2004;

Wright et al., 2006), permeability measurements of one set of rhyolitic pumices demonstrated an abrupt increase at a threshold porosity of 60% (Eichelberger et al., 1986). Rust and Cashman (2004) suggested that the significantly higher threshold in Eichelberger et al.'s (1986) observations is due to bubble deformation, bubble collapse, and the presence of crystals in some samples.

Permeability-porosity relationships in the literature are mostly derived from numerous studies of dacitic to rhyolitic volcanic rocks (e.g., Klug and Cashman, 1996; Klug et al., 2002; Wright et al., 2006; Takeuchi et al., 2008; Yokoyama and Takeuchi, 2009). However, only a few studies of basaltic rocks exist (Saar and Manga, 1999; Mueller et al., 2005; Benson et al., 2007). These show that vesicular volcanic rocks have Darcian permeabilities in the range 10^{-14} to 10^{-11} m^2 at porosities between 2 and 92%, and that the measured permeability can vary by 3 orders of magnitude at a given porosity (Klug and Cashman, 1996; Rust and Cashman, 2004; Wright et al., 2009; Yokoyama and Takeuchi, 2009). Such permeability variations have been attributed to bubble deformation and elongation (Saar and Manga, 1999), bubble sizes and distributions (Yokoyama and Takeuchi, 2009), and the tortuosity of the bubble-pore pathway (Wright et al., 2009).

Initially, reported permeabilities were based on Darcy's law (e.g., Eichelberger et al., 1986) where the pure Reynolds number, $\mathrm{Re} = \frac{\rho u L}{\mu}$ (where ρ is the density of the flow, u is the flow velocity, μ is the viscosity of the flow, and L is the length scale), was much less than 1, so inertial effects can be neglected. As flow velocity increases, fluid inertia becomes increasingly important (relative to the viscous stresses) and the flow eventually becomes dominated by inertia. In the inertial laminar flow regime, there develops a non-linear relationship between the pressure gradient and average fluid velocity. At still higher velocities, a turbulent inertial regime prevails where the microscale flow is time dependent even when subjected to steady forcing (average pressure gradient). The Forchheimer equation is generally used to study inertial flow in porous media and describes non-Darcian flow (Ruth and Ma, 1992). The Forchheimer number *Fo* (the definition of *Fo* is discussed in section 2.3), obtained from the Forchheimer equation, is

used to identify the onset of non-Darcian flow in porous media. Only a few volcanologic studies have used the Forchheimer equation to evaluate the impact of inertial effects on permeability of volcanic rocks (Rust and Cashman, 2004; Takeuchi et al., 2008; Yokoyama and Takeuchi, 2009). Note that the notation used in this thesis and the units of measurement used are listed in Table 1.1.

Direct permeability measurements on volcanic rocks are sensitive to measurement conditions, such as sample shape, size, gas flow rate, etc. (Rust and Cashman, 2004; Takeuchi et al., 2008; Wright et al., 2009). In the past decade, lattice-Boltzmann (LB) simulations have been widely used to study the transport properties of porous media (e.g., Martys and Chen, 1996; Hill and Koch, 2002; Manwart et al., 2002). This is an effective method for modeling flow through complex porous structures. However, few lattice-Boltzmann simulation studies have been undertaken to investigate flow in volcanic materials (Bosl et al., 1998; Keehm et al., 2004; Fredrich et al., 2006; Wright et al., 2006; Polacci et al., 2009).

Thus, the first object of this work is to investigate permeability development with porosity in experimentally produced, vesicular, crystal-free Stromboli basalt produced in degassing experiments at 1 atm and at 162 to 370 MPa. We compute the hydrodynamic permeability of the three-dimensional, 3-D, structures of vesicular Stromboli glasses from X-ray μCT using lattice-Boltzmann simulations, and we measure the permeability of these samples using a gas permeameter. We examine the inertial effect of flow in both lattice-Boltzmann simulated flow and gas flow through the real vesicular samples, and study the correlation between friction factor f_k and the Forchheimer number Fo. These results for our experimentally produced, vesicular glasses are compared with previous experimental measurements on volcanic rocks.

However, rocks from Stromboli contain crystals. Those crystals might influence the bubble size distributions and permeabilities. The second object of this work is to report the results of my study on the porosity permeability relationships for experimentally produced, crystal-bearing, vesicular samples, which are compared against the results of

the aphyric samples. I studied bubble formation and growth in crystal-bearing Stromboli basaltic melts with X-ray μCT at high (1.85 micron voxel edge length) and low (5.46 or 7.81 micron voxel edge length) resolution. I investigated the effect of crystals on bubble size distributions and permeability in the Stromboli basaltic magma. Based on my experimental results, I present a model to describe convection between a degassed, highly crystallized, scoriaceous magma and a poorly crystallized, volatile-rich, pumiceous magma, which have been proposed by many authors to reside in the Stromboli volcano conduit (e.g., Métrich et al., 2001, 2010). I propose that the degassed, scoriaceous magma body acts as a cap that allows bubbles to accumulate and form a foam layer at the top of the volatile-rich pumice magma body, potentially resulting in a more-violent paroxysmal explosion.

All of these results were originally written as manuscripts, which were published in the Journal of Geophysical Research (JGR) and Geophysical Research Letters (GRL). The paper in JGR was co-authored with D R Baker and R J Hill, and paper in GRL was co-authored with D R Baker, M Polacci and R J Hill. I was the first author of both papers, and I was the main contributor to these works. My coauthors helped to perform experiments, assist with LB simulations, and to edit my manuscripts by giving advice and through discussions.

Figure 1.1 Map of Stromboli island (Figure reproduced from Martino et al., 2011, *Journal of Geophysical Research* by permission of the author and the American Geophysical Union).

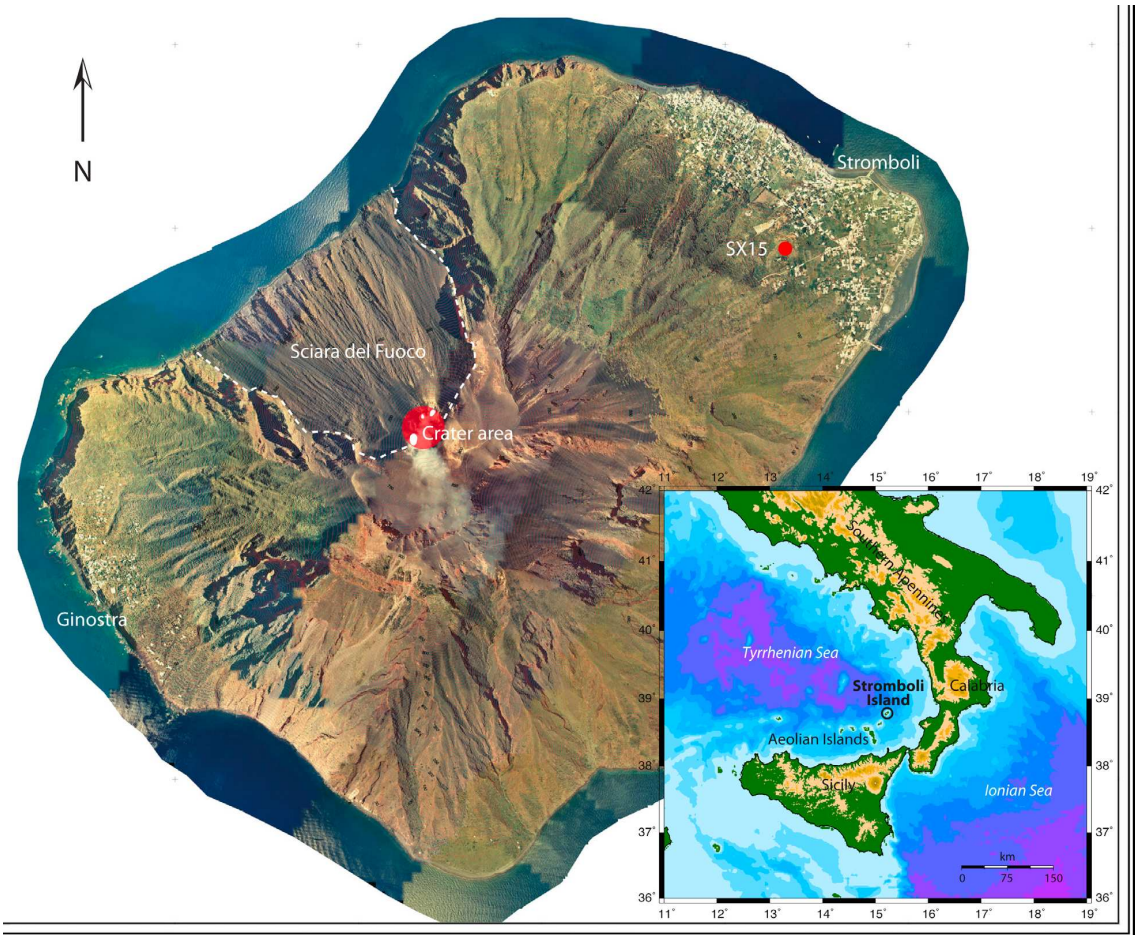

Table 1.1 Notation and description of the notation

Notation	Units	Description
a	μm	voxel size (grid resolution)
c		proportionality constant (equation (4.1))
c_1		proportionality constant (equation (5.2))
c_2		proportionality constant (equation (5.3))
D	μm	bubble diameter
D_{H2O}	$m^2\ s^{-1}$	water diffusion coefficient (equation (5.7))
$\boldsymbol{f}$		uniform body force
f_k		friction factor
Fo		Forchheimer number
g	$m\ s^{-2}$	gravity acceleration
k	m^2	Darcian permeability
k_1	m^2	Darcian permeability in Forchheimer equation
k_2	m	non-Darcian permeability in Forchheimer equation
l		characteristic length scale
L	m	sample length
n		exponent (equation (4.1))
N_L	voxel	number of voxels in the lattice
P	Pa	pressure (equation (5.7))
P_g	Pa	gas pressure
P_i	Pa	gas pressure at the inlet of the sample
P_o	Pa	gas pressure at the outlet of the sample
ΔP	Pa	differential pressure
$\langle \nabla P \rangle$		uniform pressure gradient (equation (2.4))
Q_{up}	$m^3\ s^{-1}$	volume flux of ascending magma (equation (6.3))
Q_{down}	$m^3\ s^{-1}$	volume flux of descending magma (equation (6.4))
r_a	m	radius of ascending magma flow column (equation (6.3))
r_b	μm	bubble radius (equation (5.7))
r_c	m	radius of the volcano conduit (equation (6.4))
r_{cry}	m	crystal radius

R	J mol^{-1} K^{-1}	ideal gas constant
Re		Reynolds number
S	wt%	water solubility (equation (5.7))
T	K	the absolute temperature
u_0		characteristic velocity scale
$\langle \boldsymbol{u} \rangle$		nondimensional average velocity
u_g	m s^{-1}	gas superficial velocity
u_l	m s^{-1}	fluid superficial velocity
U_c	m s^{-1}	crystal sinking velocity
V		nondimensional volume
V_{bubble}	μm^3	the total bubble volume (equation (5.1))
V_{cry}	μm^3	the total crystal volume
V_{max}	μm^3	the volume of the largest bubble (equation (5.1))
V_{melt}	μm^3	the total melt volume
α		pore geometry factor
ϕ		porosity
ϕ_{cry}		crystal volume fraction
ℓ		Brinkman screening length
μ_a	Pa s	ascending magma viscosity
μ_d	Pa s	descending magma viscosity
μ_g	Pa s	gas viscosity
μ_l	Pa s	fluid viscosity
ρ_g	kg m^{-3}	gas density
ρ_l	kg m^{-3}	fluid density
ρ_{basalt}	kg m^{-3}	basalt density (equation (6.2))
ρ_{H2O}	kg m^{-3}	H_2O density (equation (6.2))
$\rho_{l\text{-}l}$	kg m^{-3}	density difference between two magmas (equation (6.4))
σ	N m^{-1}	surface tension (equation (5.7))
δ	m	melt thickness between two bubbles (equation (5.7))
τ	s	bubble coarsening time (equation (5.7))

CHAPTER 2: CRYSTALLIZATION EXPERIMENTS, DEGASSING EXPERIMENTS AND PERMEABILITY STUDY METHODS

2.1 Degassing experiments on crystal-free samples

We prepared samples of vesicular, crystal-free Stromboli basalt glasses with porosities from 5.3 to 92.4%. The samples were synthesized by hydrating or hydrating and carbonating aliquots of the Stromboli golden pumice (erupted on April 5, 2003). The composition of this pumice in weight percent is: SiO_2 = 50.8, TiO_2 = 0.94, Al_2O_3 = 18.5, FeO = 6.38, MnO = 0.15, MgO = 6.35, CaO = 12.2, Na_2O = 2.43, K_2O = 1.89, and P_2O_5 = 0.38. The starting powder had an average grain size of 100 μm. Generally 55 to 90 mg of powder was loaded into a Pt capsule with 2.2 to 9.1 wt% H_2O and welded closed. The loaded capsules were put in a 110 ^oC oven for at least 12 hours to verify that the capsule was sealed. This heating also homogeneously distributed the water in the rock powder. We melted powder + H_2O mixtures at 1250 ^oC and 1 GPa in a piston cylinder for 1.0 or 2.0 hours. After hydration, some samples were then isothermally decompressed to between 162 and 370 MPa, and after bubble growth times of 0 to 3600 seconds the experiments were isobarically quenched to 600 °C to produce vesicular glasses. Other hydration and carbonation experiments at 1 GPa and 1250 °C were isobarically quenched, and the glasses produced in these experiments were used as starting materials for 1-atm, in-situ degassing experiments performed on the GSECARS bending magnet beamline at the Advanced Photon Source (Argonne, Illinois, USA). Details of the 1-atm in-situ degassing experiments can be seen in Bai et al. (2008). After the degassing experiments, X-ray μCT analysis was performed on the vesicular glasses at the GSECARS bending magnet X-ray beamline, and 3-D microtomographic images were used to analyze the structures, including porosity, bubble sizes, and distributions. The cubic voxel edge length ranged from 4.76 to 10.84 μm and was chosen to image the entire experimental sample.

About 100 to 400 slices from the 3-D tomographic images of each sample were analyzed using the ImageJ program (Rasband, 1997). With this software, the melt in the image is defined as the matrix component, and an individual bubble is represented by a set of voxels, defined as the bubble component. We used the threshold function to divide the image into melt and bubble components. During the thresholding process, we began with the Bright/Contrast function to increase the intensity of bubbles and decrease the intensity of matrix, and hence clearly defined the bubble and melt regions, then the threshold process was applied. The threshold was chosen to separate bubbles that appear to touch, but not overlap into individual bubbles, and to treat overlapped bubbles as a connected bubble. Note that we did not perform any "open" or "close" processes after thresholding. Both processes smooth the objects, but "open" process is an erosion operation that can remove isolated pixels while "close" process is a dilation operation that can fill in small holes, so these processes can significantly affect the apparent bubble connectivity and bubble fractions for samples with porosities over ~ 65%. Bubbles were separated and counted using the Blob3D program. The detailed procedures related to Blob3D are described by Ketcham (2005). The volumes of individual bubbles were measured, and the porosity of the samples was calculated from the sum of the bubble volumes divided by the total sample volume (bubble + glass).

Thirty-four 3-D tomographic images of samples were used for lattice-Boltzmann simulations. Four samples were produced in 162 to 370 MPa degassing experiments and 29 in 1-atm in-situ degassing experiments; additionally, one natural Stromboli basaltic pumice was studied. Full tomographic images could not be used for lattice-Boltzmann simulations because of our computer limitations. These subvolumes of the tomographic images were cropped for the simulations. The grid sizes N_L of most simulation samples were in the range 160 to 240 voxels along each edge; only one sample had 100 voxels along each edge, and it had a porosity below 30%. Two of the porosities of the subvolumes measured for simulations were about 10% higher than the porosities of the entire samples measured by X-ray μCT, but in most high-porosity samples the difference is within ~ 4%. This difference is caused by heterogeneous bubble distributions; the bubble size and bubble number density were lower at the edges of some samples. When

we prepared the simulation samples, we generally cropped the center of the complete tomographic images where the highest bubble number density occurs; thus, the porosities of subvolumes for simulations can be higher than the total porosities of the original samples measured by X-ray μCT.

2.2 Crystallization and degassing experiments on crystal-bearing samples

The experiments were performed in two steps: crystal growth experiments at high pressure and in-situ degassing experiments in crystal-bearing melts at 1 bar. The starting materials were the same finely ground basalt power of the Stromboli golden pumice (erupted on April 5, 2003). Platinum capsules were loaded with rock power and water and welded following the same procedures as used for the crystal free experiments described above. These capsules were placed in a piston-cylinder apparatus and the powder + H_2O mixtures melted at 1 GPa for 1.0 hour, then the temperature was reduced to the crystallization temperature at a cooling rate of 1 ^oC/min (Table 2.1). After the samples were held at the crystallization temperature for 6 to 27 hours, the experiments were isobarically quenched to room temperature. 3-D crystal size distributions in these quenched glasses were analyzed using X-ray μCT on the GSECARS beamline at the Advanced Photo Source in Argonne, Illinois, USA. The X-ray beam from the bending magnet source had an energy of 25 keV. The voxel edge-length during X-ray μCT was 5.22 μm. Then, we sectioned these glasses into chips for in-situ degassing.

The in-situ degassing experiments were performed on the GSECARS bending magnet beamline at 1 atm, as described in detail by Bai et al. (2008). After bubble formation and growth for ~ 10 min, the samples were quenched before bubbles popped. The quench temperatures were in the range of ~ 713 to 1200 ºC. The durations of the degassing experiments varied from ~ 10 to 15 min.

The 3-D crystal and bubble size distributions in the degassed samples were studied by X-ray μCT on the GSECARS beamline at the Advanced Photon Source with an edge-

length voxel size of 5.46 to 7.81 μm. To investigate the effect of tomographic resolution, we also performed X-ray μCT on these samples and natural scoria from Stromboli basalt at the Tomcat beamline of the Swiss Light Source, Villigen, Switzerland, with voxels of 1.85 μm edge-length. The X-ray energy used for microtomography was 25 kev. We separated the bubbles and crystals respectively from the melt with ImageJ (Rasband, 1997) and the Blob3D programs (Ketcham, 2005), and measured the crystal and bubble volumes as described above for the crystal-free experiments. The 3-D tomographic image set collected at 5.46–9.0 μm was studied entirely, but we cropped the tomographic images of experimental samples imaged at 1.85 μm into volumes of $1000 \times 1000 \times 800$ to $1412 \times 1476 \times 1110$ voxels; these volumes are large enough to contain enough bubbles and crystals to be representative samples. Because crystals in the natural scoria samples can be up to between 0.3 and 0.56 mm^3, we cropped the tomographic images of the natural samples into $1968 \times 1993 \times 1200$ to $2044 \times 2044 \times 997$ voxel volumes that were large enough to contain most crystals and vesicles. Then we thresholded the images into binary images with ImageJ, and separated the crystals from the melt with the Blob3D program. During the crystal thresholding process, because the crystal intensities are similar to the bubble intensities, we varied the threshold value to constrain the pixels of crystals and bubbles, then performed the "open" function to get rid of the bubble pixels, and the performed the "dilate" and "fill holes" function to obtain the best separation of the crystals in the binary images. We calculated the total crystal volume fraction in the samples as $\phi_{cry} = \frac{V_{cry}}{V_{cry} + V_{bubble} + V_{melt}}$. The uncertainty in ϕ_{cry} is within 2 to 4.3%. The porosity was determined as $\phi = \frac{V_{bubble}}{V_{cry} + V_{bubble} + V_{melt}}$. The uncertainty in ϕ is within 3.1 to 5.0%. Note that the uncertainty is determined by calculating the standard deviation of ϕ_{cry} or ϕ of the samples.

2.3 Permeability study methods

2.3.1 Defining permeability in porous media

The Darcian permeability of a compressible fluid can be defined by (Innocentini et al., 2000; Yokoyama and Takeuchi, 2009):

$$\frac{P_i^2 - P_o^2}{2P_g L} = \frac{\mu_g}{k} u_g \tag{2.1}$$

where k (m^2) is termed the Darcian permeability of a sample, P_i (Pa) and P_o (Pa) are the gas pressure at the inlet and outlet of the sample of length L (m). P_g (Pa) is the gas pressure at which the gas flow is measured. μ_g (Pa s) is the gas shear viscosity, and u_g (m/s) is the gas superficial flow velocity. Note that for an incompressible fluid, the left-side of equation (2.1) that represents the pressure gradient can be simplified to $\frac{P_i - P_o}{L} = \frac{\Delta P}{L}$. In the case of Darcian flow, fluid inertia is negligible and the applied pressure gradient is linearly dependent on the gas superficial flow velocity. To study the permeability of porous samples with fluid inertia, we adopt the one-dimensional Forchheimer equation (Ruth and Ma, 1992; Rust and Cashman, 2004):

$$\frac{P_i^2 - P_o^2}{2PL} = \frac{\mu_l}{k_1} u_l + \frac{\rho_l}{k_2} u_l^2 \tag{2.2}$$

where k_1 (m^2) is the Darcian (viscous) permeability, k_2 (m) is the non-Darcian (inertial) permeability, μ_l (Pa s) is the fluid viscosity, and u_l (m/s) is the fluid velocity. $\frac{\mu_l}{k_1} u_l$ in (2.2) represents the contribution of the viscous friction between fluid layers and the pore wall, and $\frac{\rho_l}{k_2} u_l^2$ in (2.2) represents the contributions of inertia and turbulence (Ruth and Ma, 1992). Equation (2.2) can be written as:

$$\frac{P_i^2 - P_o^2}{2PL} = \frac{\mu_l}{k_1} u_l (1 + Fo) \tag{2.3}$$

where $Fo = \frac{\rho_l u_l}{\mu_l}\left[\frac{k_1}{k_2}\right]$ is the Forchheimer number, which is analogous to the *Re* number and compares inertial and viscous contributions to the dissipation. The inertial effects are negligible when $Fo << 1$, in which case equation (2.3) reduces to the Darcy's equation (2.1), and k_1 equals to Darcian permeability k. If $Fo >> 1$, inertial effects are present, and the non-Darcian permeability k_2 dominates. In this case, either u_l or $\frac{k_1}{k_2}$ increases, implying that the fluid velocity and pore structure influence the inertial effects. Thus, *Fo* represents the ratio of inertial to viscous forces resisting fluid flow, and indicates when microscopic inertial effects lead to significant macroscopic effects. Corresponding to the increasing inertial effects and variations of *Fo*, four major flow regimes have been identified (Dybbs and Edwards, 1984; Wood, 2007): Darcian flow occurs when $Fo << 1$; transition flow (Forchheimer flow) dominated by inertial effects occurs when $1 \sim 10 < Fo < 150$; unsteady Darcian flow exists when $150 < Fo < 300$, this flow regime is characterized by the occurrence of wake oscillations and development of vortices in the flow profile; and turbulent flow occurs when $Fo > 300$. However, because different systems display different pore geometries, these *Fo* ranges may vary significantly; thus, as discussed in later part, we introduce the friction factor, f_k, to better delineate the flow regime.

2.3.2 Lattice-Boltzmann simulations

Exact numerical calculation, such as Lattice-Boltzmann simulation, is an effective way to study permeability of porous material, because experimental micropermeametry is costly and inaccurate (Manwart et al., 2002). Lattice-Boltzmann simulations provide approximate solutions of the incompressible Navier-Stokes equations on macroscopic length and time scales (Martys and Chen, 1996; Hill and Koch, 2002; Manwart et al., 2002). The lattice-Boltzmann method models fluid particles on a lattice at discrete time steps. The evolution of the particle velocity distribution consists of a collision step followed by a streaming step, which relaxes the fluid-particle velocity distribution function toward equilibrium. Population densities correspond to velocities in directions to the 6 nearest and 12 next-nearest neighbouring lattice nodes (cubic lattice). The

individual particle interactions meet the requirements of mass and momentum conservation at each lattice node. The pressure and velocity are obtained from the zeroth and first moments of the fluid-particle velocity distribution function and the equation of state relating the density to the pressure. The lattice-Boltzmann program in this study is a slightly modified version of that used by Hill et al. (2001) and Hill and Koch (2002).

In our simulations, the sample, composed of fluid and solid domains, is subjected to a uniform body force (per unit volume) $\boldsymbol{f}$ with triply periodic boundary conditions (Hill et al., 2001; Hill and Koch, 2002). This is equivalent to driving the fluid through the pores by a uniform pressure gradient $\langle \nabla P \rangle$. For the Darcian permeability, we ensure that the body force is weak enough to drive a steady viscous flow with a pore-scale Reynolds number $\mathrm{Re} = \dfrac{u_0 l}{\dfrac{\mu_l}{\rho_l}} << 1$. Here, u_0 and l are characteristic velocity and length scales, and $\dfrac{\mu_l}{\rho_l}$ is the kinematic viscosity. Under low-Reynolds-number conditions, the average (superficial) velocity $\langle \boldsymbol{u} \rangle$ is linear in $\langle \nabla P \rangle$, i.e.,

$$\langle u \rangle = -\frac{\ell^2}{\mu_l} \langle \nabla P \rangle \tag{2.4}$$

Here, the microstructure is assumed to be statistically isotropic, so the Darcian permeability tensor is isotropic with a scalar permeability $\dfrac{\ell^2}{\mu_l}$ (ℓ is Brinkman screening length, and μ_l is the fluid shear viscosity). To emphasize the purely geometrical characteristics of the permeability, we report the Darcian permeability as the square of the Brinkman screening length ℓ^2 (Brinkman, 1947) averaged from simulations with $\langle \nabla P \rangle$ directed along each of the three principal axes of each sample, i.e., X-, Y-, and Z-directions. With $u_0 \approx \dfrac{\langle u \rangle}{\phi}$ and $l \approx \ell$, we verified that $\mathrm{Re} \approx \dfrac{\langle u \rangle \ell}{\phi \dfrac{\mu_l}{\rho_l}} << 1$, and that $\langle \boldsymbol{u} \rangle$ is linear with respect to $\langle \nabla P \rangle$.

The ability of simulations to predict the macroscale Darcian permeability is limited by two independent characteristics. The first is the intrinsic grid resolution, as measured by the physical voxel size a with respect to the characteristic length of the pores (e.g., as determined by bubble size, surface curvature and surface roughness). The second is the physical sample size (quantified by the product of the number of lattice points along each edge N_L and the voxel size a), with respect to the geometrical correlation length (e.g., as determined by bubble connectivity and volume fractions) (Hill et al., 2001; Harting et al., 2004).

In this study we did not quantify the anisotropy of the permeability. We performed the LB simulations with the mean pressure gradient directed along X-, Y-, Z-directions of cubic tomographic images of samples, so the permeabilities are determined along the X-, Y-, Z-directions. Note that the flux is not necessarily in the direction of the applied pressure gradient (Hill et al., 2001; Hill and Koch, 2002). Nevertheless, permeability variations in the X-, Y-, Z-directions in 30 out of 34 of the crystal-free samples are within one order of magnitude. Our tomographic images show that bubble sizes and distributions did not exhibit anisotropy, except in the natural sample. Therefore we conclude that the anisotropy of the permeability in the simulations is not significant.

2.3.3 Permeability measurement techniques

The permeabilities were directly measured on a GP-100-G-M gas permeameter manufactured by Porous Materials Inc (PMI). The samples were mounted in an epoxy plate with a diameter of 10 cm. Most samples were ground to 0.6 to 2 mm in thickness. To determine the area, the samples were scanned and the nearly circular cross-sectional areas were measured using ImageJ. We calculated the equivalent circular diameters based on the cross-sectional areas. Samples were mounted on an adapter plate between two O-rings in the sample chamber. The gas flow was controlled by a pressure regulator and the gas used was dry air. The air has a density 1.204 kg/m^3 and a viscosity 1.85×10^{-5} Pa s at a room temperature of ~ 20 ^{o}C.

Table 2.1 Crystallization experiments and results[a]

Run	H_2O concentration (%)	Crystallization Temperature (ºC)	Growth Time (h)	Phase assemblage[b]	ϕ_{cry}
Bt3	2.4	1125	8	plg, gl	<5
Bt4	3.2	1125	8	plg, gl	<5
Bt11	2.6	1115	16.5	plg, cpx, gl	<5
SC23	6	1115	16.5	plg, spl, gl	47
Bt21	4	1100	27	plg, cpx, gl	<10
Bt22	2.5	1100	27	plg, cpx, gl	<10
Bt5	3.6	1100	18.4	plg, cpx, gl	38.8
Bt7	2.4	1100	18.4	plg, cpx, gl	41.6
Bt8	3.2	1100	17.8	plg, gl	<5
SC22	9.9	1100	17.8	plg, gl	<2
Bt1	2.7	1100	16	plg, gl	42.9
Bt9	3.9	1100	16	plg, gl	<5
Bt13	2.9	1100	10	plg, gl	<2
Bt14	3.7	1100	10	plg, gl	<5
SC21	9	1100	10	plg, gl	<5
Bt20	3.1	1100	8	plg, cpx, gl	<10
Bt17	3.2	1100	7.5	cpx, gl, spl	48.3

[a]Parameters are ϕ_{cry}, crystal volume fraction in the melts ($\phi_{cry} = V_{cry}/(V_{cry} + V_{melt})$, where V_{cry} is the total crystal volume, and V_{melt} is the total melt volume.

[b]The terms are plg = plagioclase; cpx = clinopyroxene; gl = glass; spl = spinel.

CHAPTER 3: INVESTIGATING THE EFFECTS OF SAMPLE SIZE AND RESOLULTION ON POROSITY AND PERMEABILITY

3.1 Sample size effects on permeability from lattice-Boltzmann simulations

A visualization of a representative lattice-Boltzmann simulation is presented in Figure 3.1. This shows the steady dimensionless velocity field in sample St25a with a porosity of 87.4%. The size of this simulation is 200 × 200 × 200 voxels, where each voxel has an edge length of 8.11 μm. In the crystal-free samples, where the bubble number density is low and the binary tomography images only consist of bubbles and melt, we can perform simulations on samples of up to 200 to 240 voxels along each edge. However, in the crystal-bearing samples, the bubble number density is larger than the crystal-free samples and more bubbles need more computer memory, so we generally can perform simulations only on samples of up to 180 to 210 voxels along each edge because of the computer memory. So we chose the crystal-free samples to test the simulation sample size effects.

In this study, N_L, the number of voxels along each dimension of the cubic volume used for the lattice-Boltzmann simulations, varied from 30 to 240 voxels with a fixed voxel size a (grid resolution) between 4.76 and 10.84 μm to test the simulation sample size effects. These simulations probe spatial correlations in the microstructure with a fixed pore-scale hydrodynamic resolution.

At low porosities the permeability decreases with increasing sample size, N_L, at a constant voxel size, and becomes independent of the sample size when $N_L a > 761.6$ μm (Figure 3.2a). The most significant effect of reducing the lattice-Boltzmann simulation sample size is to increase the calculated permeability by a factor of about 20. The sample size effect on permeability is insignificant at porosities over ~ 65% in our simulations, because the bubble distributions tend to be homogenous. Because most of our samples

have $N_L a$ dimensions over 761.6 μm, the effect of sample size on the calculated permeability is negligible.

3.2 Resolution effects on porosity and calculated permeability

Because each sample was only imaged at the best resolution to scan the entire sample, 7 to 10.84 μm for large samples and 4.76 to 4.85 μm for the small samples, the grid resolution effect was investigated by coarsening the grid. This was done by varying a with fixed $N_L a$. During coarsening processes, N_L was decreased by averaging and reducing 8, 64, or 512 voxels of a sample to a single coarse-grained voxel.

No obvious trend between the calculated permeability and the voxel resolution was found. Grid coarsening tests (i.e., varying the voxel size a) show that permeability variations are more sensitive to grid resolution at porosities below the sphere percolation threshold of ~ 29 volume percent (Figure 3.2b and Table 3.1). The permeability decreases with increasing grid resolution. However, grid resolution appears to have no effect on the calculated permeability at porosities between approximately 65 and 94%. This implies that the effect of grid resolution on the calculated permeability is negligible at these high porosities.

To further investigate the voxel resolution effect on the bubble size and porosity, we performed X-ray μCT on the same crystal-free samples with a low resolution of 5.46 to 7.81 μm voxel edge-length at the Advanced Photon Source, and with a higher resolution of 1.85 μm voxel edge-length at the Swiss Light Source. Samples imaged at 1.85 μm display ~ 150–450 more small bubbles of the order of 10^{-7} mm^3 than imaged at 5.46–7.81 μm; these small bubbles are generally distributed in the melt pockets between larger bubbles, and they are not connected with the larger bubbles. Despite the differences in resolution the porosities measured in the same samples imaged at high- and low-resolution are within 4%, and the bubble size distributions display the same trends (Figure 3.3). This suggests that voxel sizes of X-ray μCT do not significantly affect the bubble sizes and porosities determined in this study.

To investigate the effect of voxel size on permeability, we performed LB simulations on 4 samples imaged at 5.46–7.81 μm and at 1.85 μm (Table 3.2). Prior to the simulations, we cropped the same part of the tomographic images of samples that were imaged at 5.46–7.81 μm and at 1.85 μm to obtain the same bubble geometry. The porosity differences between the same samples imaged at low- and high-resolution are within 2.4%. Simulations performed on three samples show that varying the resolution only affects the permeability by less than 1 order of magnitude. The exception is the fourth sample, Bt20, whose permeability based upon low resolution images is about 1 order of magnitude higher than when high resolution images are used. Bt20 has a ϕ of ~ 90%, most bubbles are connected due to coalescence, and some thin bubble walls may easily be detected as ruptured walls during thresholding. This artifact might produce its higher calculated permeability, but considering that the measured permeability of this sample is close to both the permeability calculated at low- and high-resolution, this resolution effect is minor. Thus, the resolution effect on the calculated permeability is not significant in our studies.

The resolution effect on the calculated permeability is also supported by the similarity of the measured permeability and the calculated permeability, showing that the difference between the measured permeability and the calculated permeability from most samples is within one order of magnitude. See next chapter for further details.

Figure 3.1 Dimensionless velocity from a lattice-Boltzmann simulation of flow in sample St25a with a porosity of 87.4% (Figure reproduced from Bai et al., 2010, *Journal of Geophysical Research* by permission of the American Geophysical Union).

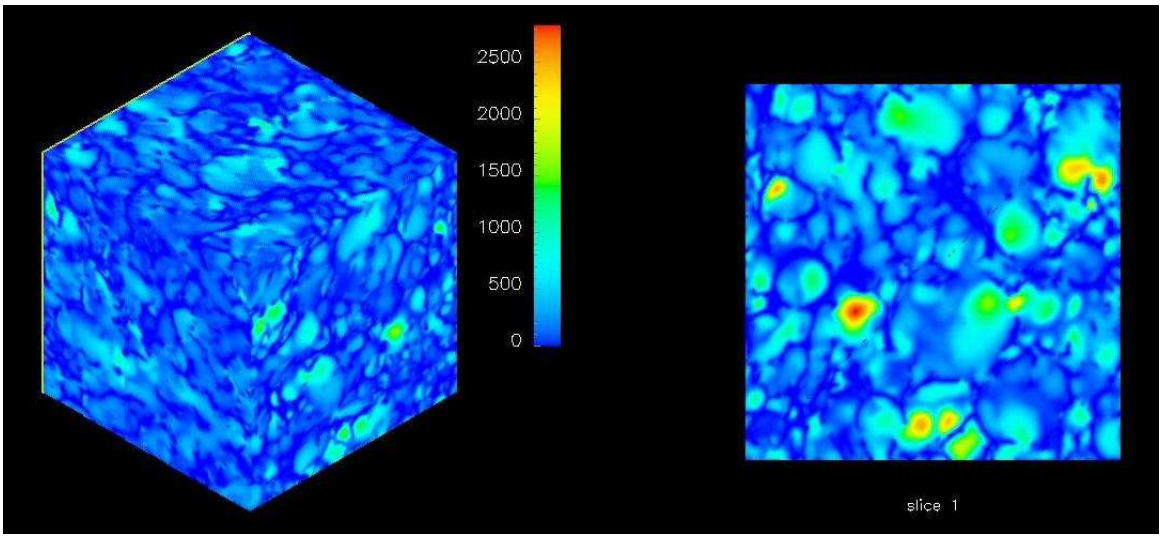

Figure 3.2 Calculated permeabilities for the samples, but with different simulation sizes (**a**) and with different grid sizes produced from the coarsening process (**b**). The standard deviations of uncertainties are indicated by the error bars for each point. Note that X-axis is the edge length of simulation samples (N_L) multiplied by the resolution of samples (a) (Figure reproduced from Bai et al., 2010, *Journal of Geophysical Research* by permission of the American Geophysical Union).

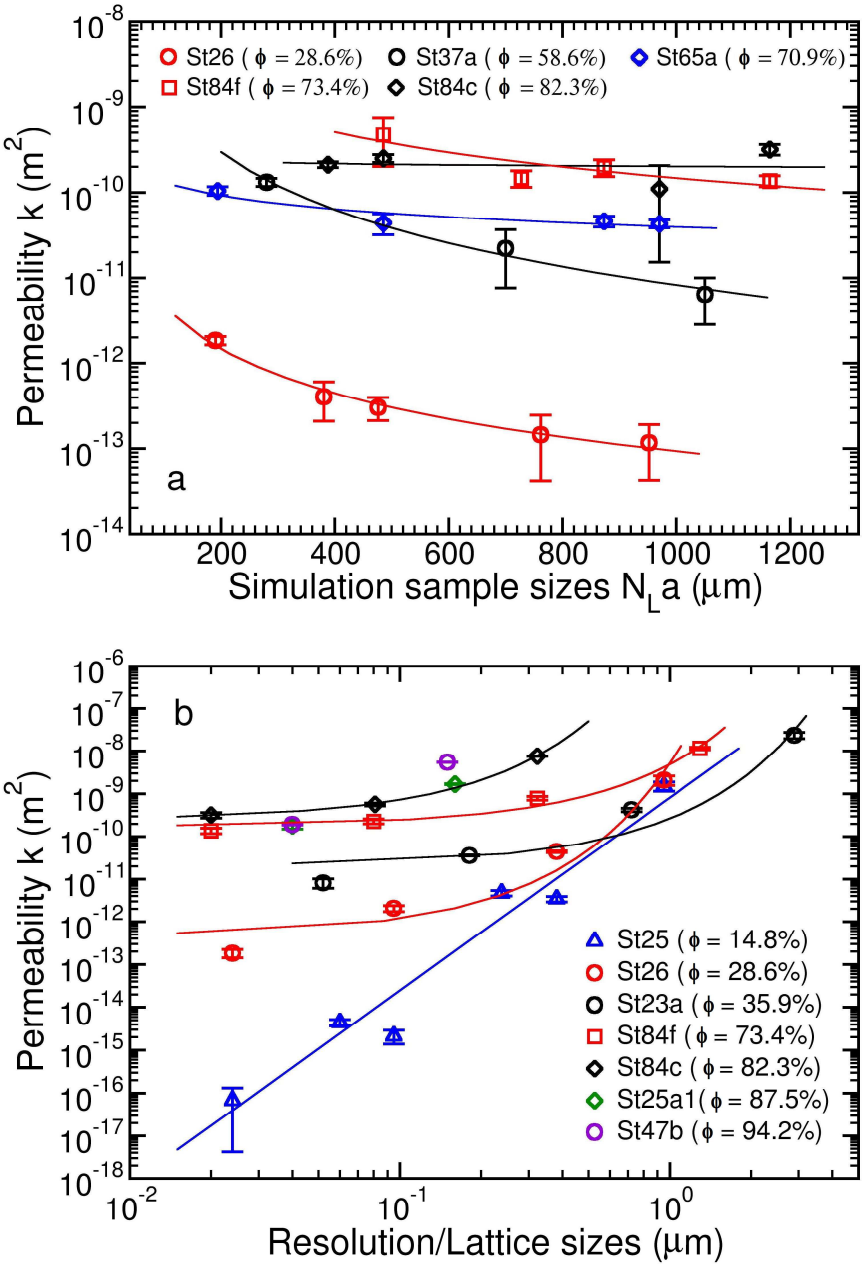

Figure 3.3 3-D cumulative (open circles) and non-cumulative (bars) bubble size distributions of sample Bt1b imaged at high resolution (black symbol) and low resolution (green symbol). *a* is resolution. The uncertainties in ϕ are within 3.1 to 5.0% as discussed in section 2.2 (Figure reproduced from Bai et al., 2011, *Geophysical Research Letters* by permission of the American Geophysical Union).

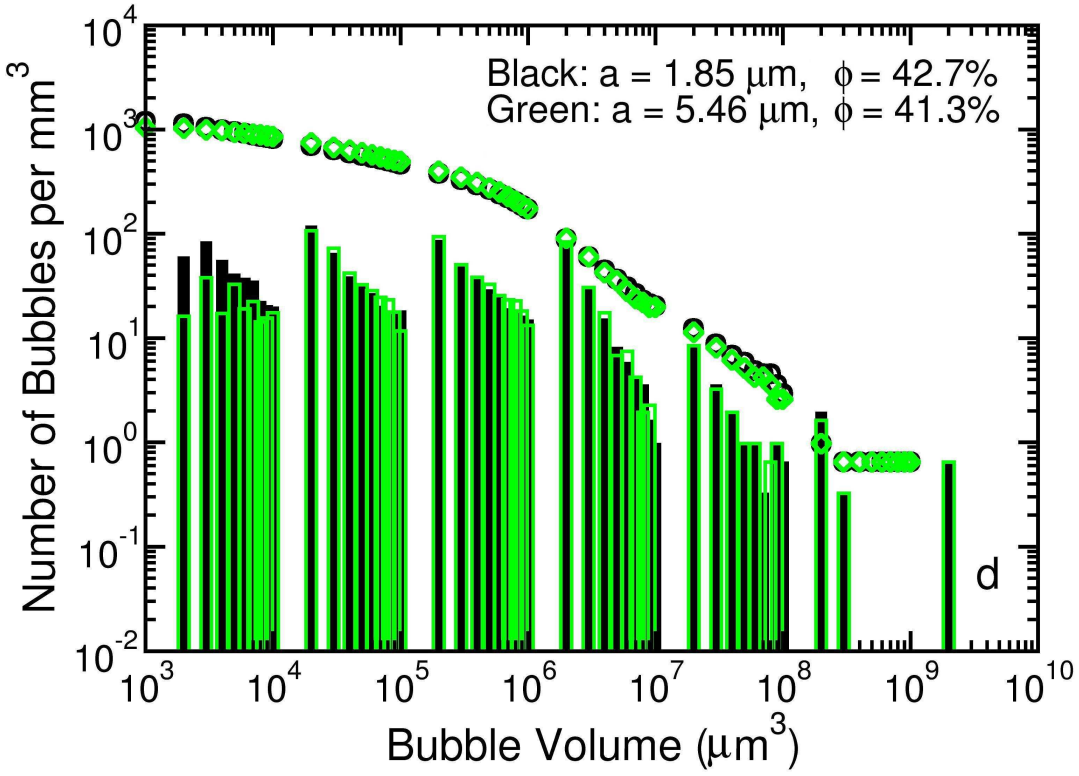

Table 3.1 Simulation results from coarsened samples[a]

Sample	a (μm)	N_L (voxels)	k (m^2)	Re
St26[b]	4.76	200	1.82×10^{-13}	1.75×10^{-10}
	9.52	100	2.05×10^{-12}	1.50×10^{-9}
	19.04	50	4.45×10^{-11}	2.38×10^{-8}
	38.08	40	2.09×10^{-9}	4.05×10^{-7}
St84f[c]	4.76	240	1.37×10^{-10}	5.91×10^{-8}
	9.52	120	2.28×10^{-10}	9.69×10^{-8}
	19.04	60	7.87×10^{-10}	2.87×10^{-7}
	38.08	30	1.15×10^{-8}	3.64×10^{-6}

[a]Parameters are a, the voxel size (grid resolution); N_L, the lattice number along each edge of simulation sample; k, calculated Darcian permeability; Re, Reynolds number, $\mathrm{Re} = \frac{\langle u \rangle \ell}{\phi \frac{\mu_l}{\rho_l}}$, where ℓ is the value of Brinkman screening length when $Re \to 0$ (see details in the text).

[b]The porosity of the subvolume of this sample used for measurement before coarsening is 28.5%.

[c]The porosity of subvolume of this sample (natural sample) used for measurement before coarsening is 73.4%.

Table 3.2 Permeability simulation results from samples imaged with different voxel sizes[a]

Sample	a (μm)	N_L(voxels)	ϕ (%)	k (m^2)
Bt1b	1.85	240	31.1	$4.08 \pm 0.51 \times 10^{-15}$
	5.46	160	33.5	$4.85 \pm 3.57 \times 10^{-15}$
Bt5b	1.85	240	54.3	$1.55 \pm 1.2 \times 10^{-11}$
	5.46	120	52.2	$5.21 \pm 3.47 \times 10^{-12}$
Bt17a	1.85	240	67.5	$2.84 \pm 0.35 \times 10^{-11}$
	5.46	240	66.0	$1.59 \pm 0.38 \times 10^{-11}$
Bt20	1.85	240	90.3	$8.91 \pm 1.72 \times 10^{-11}$
	7.81	240	89.1	$6.54 \pm 1.58 \times 10^{-10}$

[a]Parameters are a, the voxel size (grid resolution); ϕ, porosity of the tomographic images; N_L, lattice number (voxels) along each edge of simulated samples; k, Darcian permeability.

CHAPTER 4: PERMEABILITY RESULS FROM MEASUREMENTS AND LATTICE-BOLTZMANN SIMULATIONS

4.1 Darcian permeability of crystal-free samples from lattice-Boltzmann simulation and measurements

4.1.1 Permeability-porosity relations

The calculated permeabilities from simulations and the measured permeabilites of the crystal-free samples are listed in Table 4.1. The permeability development with porosity from lattice-Boltzmann simulations and measurements is presented in Figure 4.1a. Note that all the permeabilities from LB simulations in this figure are Darcian permeabilities, corresponding to $Re \rightarrow 0$. The Darcian permeabilities from simulations range from 10^{-17} to 10^{-14} m^2 below a porosity ~ 29%; and they increase markedly at a porosity ~ 29%, reaching ~ 10^{-13} to 10^{-9} m^2 at porosities ~ 65 to 94.2%.

The permeability-porosity relationships can be fit with a Kozeny-Carman relationship between permeability k and porosity ϕ (e.g., Eichelberger et al., 1986; Klug and Cashman, 1996; Saar and Manga, 1999):

$$k(\phi) = c\,\phi^{n} \qquad (4.1)$$

where c is a proportionality constant that depends on the square of the pore radius and the tortuosity of flow path, and the exponent n depends on sample size, pore size, distribution, shape, as well as the spatial arrangement of pores (Yokoyama and Takeuchi, 2009). Our lattice-Boltzmann simulations yield $n = 6.12 \pm 0.88$.

The measured permeability data can be fit with the same equation, but $n = 4.95 \pm 0.5$. The difference in exponents between simulations and measurements is not significant; both are close to 5 when considering fitting uncertainties. We then fitted the permeability

using the same exponent n = 5. The fitting results show that $k(\phi) = 2.35 \times 10^{-20}\ \phi^5$ for LB simulations and $k(\phi) = 5.33 \times 10^{-21}\ \phi^5$ for measurements (Figure 4.1a). The exponent n derived from LB simulations and measurements is higher than that in the natural volcanic rocks (Klug and Cashman, 1996; Rust and Cashman, 2004; Wright et al., 2009; Yokoyama and Takeuchi, 2009) which shows that the exponent n is in the range of ~ 2 to 3.5.

The higher value of the exponent n found in this study may be attributed to the differences in the sample size, pore size, pore shape, and the spatial arrangement in our synthesized samples and those in the natural samples (Klug and Cashman, 1996; Saar and Manga, 1999; Wright et al., 2009 ; Yokoyama and Takeuchi, 2009). Perhaps most importantly, bubble elongation or bubble deformation is not observed in our samples. In the natural rocks, the pore is deviated from spherical to elongated or flattened to form ellipoids, resulting in the lower exponent n (Saar and Manga, 2002 ; Yokoyama and Takeuchi, 2009).

The simulated permeabilities are about half an order of magnitude higher than the measured permeabilities. This is attributed to the smaller volumes of samples used in the LB simulations. As pointed out above, most LB simulation subvolumes were cropped from the full tomographic images of samples where the highest bubble number density occurs, so the bubble connectivities and bubble apertures in some subvolumes of simulation samples are higher than those in the total samples. This can be identified in our tomographic images of the samples. Additionally, the smallest bubbles might be not detected due to the resolution of the tomographic imagery. However, our samples analyzed using X-ray μCT with resolution of 1.85 μm at the Swiss Light Source demonstrate that these smallest bubbles are ~ 4 to 10 μm in diameter, and they are generally distributed in the melt pockets between larger bubbles. The total porosity of these small bubbles is less than ~ 2%, and these small bubbles have not coalesced with the larger bubbles, consistent with SEM images of samples used in this study (Figure 4.2 and Bai et al., 2008). Therefore they will not significantly affect the permeability.

Our results conclusively demonstrate that permeability increases markedly as the percolation threshold for spheres is approached, and permeabilities attain values ~ 10^{-10} m^2 at porosities over 65%. Our studies indicate a threshold value of approximately 29 volume percent where the permeability increases by several orders of magnitude; this threshold is close to the percolation threshold for spheres of two different sizes (Consiglio et al., 2003). Thus, we also fit the permeability-porosity relationship by cutting it off below the porosity of 29% (Figure 4.1b).

4.1.2 Forchheimer permeability constants k_1 and k_2

Examples of the pressure gradient versus flow velocity from permeability measurements are shown in Figure 4.3a. Note that the flow velocity was obtained by dividing the flow rate by the cross-sectional area. Each pressure difference versus velocity curve follows a quadratic relationship at velocities > ~ 0.4 to 1 m/s, and follows Darcy's law at low velocities < ~ 0.4 m/s. This curve indicates the presence of inertial effects. The permeability constants k_1 and k_2 were obtained by fitting equation (2.2) to the experimental data (Table 4.1).

To further discriminate between Darcian and non-Darcian flow regimes, we plot the Forchheimer equation in the form:

$$\frac{P_i^2 - P_o^2}{2PLu_l^2} = \frac{\rho_l}{k_2} + \frac{\mu_l}{k_1}\frac{1}{u_l} \tag{4.2}$$

The experimental data of representative samples are plotted in Figure 4.3b where the approach to a constant at high u_l indicates non-Darcian flow. Because we can calculate $\frac{k_1}{k_2}$ based on the non-linear fitting of equation (2.2), we determine $Fo = \frac{\rho_l u_l}{\mu_l}\left[\frac{k_1}{k_2}\right]$ for each velocity. The results show that *Fo* has values of about 1 to 3 for samples with porosities less than approximately 65%, and about 3 to 6 for high porosity (> ~ 65%) samples. When *Fo* = 1, there are equal viscous and inertial contributions to flow (*Ruth*

and Ma, 1992). We use $\frac{k_1}{k_2}$ to evaluate the critical flow velocity u_{cr} at $Fo = 1$. Our results show that u_{cr} is in the range ~ 0.5 to 1 m/s.

The relation between k_1 and k_2 was found to be: $k_1 = 4.97 \times 10^{-5} k_2^{1.06}$ or $k_2 = 1.11 \times 10^4 k_1^{0.94}$, indicating that k_1 and k_2 are linearly correlated (Figure 4.4a). Similar relationships between k_1 and k_2 were previously reported in permeability measurements of natural pumices (Rust and Cashman, 2004; Yokoyama and Takeuchi, 2009) (Figure 4.4a). In our study there is no obvious correlation between $\frac{k_1}{k_2}$ and porosity. As $\frac{k_1}{k_2}$ is not a direct measurement of the bubble texture length scale (Rust and Cashman, 2004), it is necessary to constrain k_1 and k_2 with other parameters. Yokoyama and Takeuchi (2009) suggest that permeability is strongly dependent on the pore size. We therefore seek a relationship between pore size and either k_1 or k_2.

Accordingly, we further constrain the relations between permeability and pore size by measuring bubble sizes from X-ray μCT. For samples degassed between 160 and 370 MPa, all bubble size distributions have exponential bubble size distributions, and bubbles tend to be of similar sizes in most samples. Thus, we can define a meaningful average bubble size from our X-ray tomographic analysis. For samples degassed at 1-atm, the bubble size distributions tend to display power-law relations due to multiple bubble nucleation events, but bubble size distributions tend to evolve into exponential distributions at porosities over ~ 65%, and at the highest porosities investigated an interconnected foam is formed by many bubbles of spherical shape that coalesced (Figure 4.2 and Bai et al., 2008). For these high porosity samples with power-law bubble size distributions, the permeability is dominated by the connected bubbles forming the foam, thus we can neglect the secondary bubbles when determining the average bubble size. Note that connected bubbles in the foam tend to have the same size at porosities greater than ~ 65%. Therefore, we separated the bubbles in the foam into individual bubbles using Blob3D and determined their average bubble size. Comparison of k_1 or k_2 versus

bubble diameter D (μm) reveals that they display a power-law relation with exponents of 3.72 and 3.28 (Figures 4.4b and 4.4c):

$$k_1 = 9.28 \times 10^{-20} D^{3.72}$$
$$k_2 = 3.24 \times 10^{-14} D^{3.28}$$

In our study we did not perform sensitivity analysis on the parameters. Our results show that both k_1 and k_2 increase with increasing bubble diameter D, but k_1 varies by ~ 10^{-20} orders of magnitude, k_2 varies by ~ 10^{-14} orders of magnitude (Figures 4.4b and 4.4c), suggesting k_2 is more sensitive to bubble size than k_1.

4.2 Crystal and bubble size distribution, bubble number density, and permeability in crystal-bearing samples

4.2.1 Crystal sizes and distributions

Crystal fractions, ϕ_{cry}, measured from the X-ray μCT are listed in Table 2.1. We did not count each crystal type separately because the X-ray contrast between crystals was too small for accurate thresholding. However, we chose 6 samples for electron microprobe analysis of crystals at McGill University. The dominant crystals in the experimental samples are plagioclase (plg) and clinopyroxene (cpx); spinel (spl) is also observed in some samples. The relative proportions of each crystal in the crystalline assemblage of the samples are: Bt1a (plg = 0.9, cpx = 0.1); Bt5b (plg = 0.6; cpx = 0.4); Bt7R (plg = 0.55; cpx = 0.45); Bt17c (plg = 0.9, cpx = 0.1); Bt27 (plg = 0.55; cpx = 0.45); and SC23a (plg = 0.9, cpx = 0.08, spl = 0.02). We did not observe any olivine in the analysed run products, although it is found in the natural samples (Métrich et al., 2005; Armienti et al., 2007). The lack of olivine may be due to the high pressure conditions of crystal growth used in this study, which are necessary to dissolve high concentrations of water in the melt. Alternatively, it is possible that olivines in the experiments are too small and too rare to find and analyze with the electron microprobe. Also, because we did not perform microprobe analysis on all run products, we cannot exclude the possibility that olivine occurs in other samples.

Only 5 of 17 crystallization experiments produced ϕ_{cry} of 38.8–48.3%, similar to natural Stromboli samples; the other experiments produced ϕ_{cry} below 10%. Crystals in Bt1, Bt17, and SC23 range from 10^{-6} to 10^{-4} mm^3 in volume; they are elongated, and have skeletal shapes, indicative of rapid growth far from equilibrium (Lofgren, 1980). Crystals in Bt7 and Bt5 are larger, from 10^{-5} to 10^{-2} mm^3; they show tabular to granular shapes, indicative of growth at near-equilibrium conditions (Lofgren, 1980). After degassing, the crystal number density (*CND*, i.e., the number of crystals per unit volume of melt) is 743–3547 mm^{-3} (Table 4.2). Some large crystals were broken into small ones during degassing because of bubble expansion, but still retain their skeletal shapes (Figures 4.5c and 4.5d). 3-D crystal size distributions in the degassed samples generally display exponential relations in the volume range from 10^3 to 10^7 μm^3, and tend to evolve to a power-law above 10^7 μm^3 because of crystal intergrowths (Figures 4.6a and 4.6b). Natural scoria has a similar 3-D crystal size distribution type (Figures 4.6c and 4.6d). Most crystals in scoria have tabular shapes, and crystal volumes vary from 10^{-2} to 10^{-1} mm^3. Crystal networks are common in the scoria; ϕ_{cry} varies from 22.3 to 47.3%, which is generally higher than those in experimental samples. However, the *CND* in scoria varies from 26 to 90 mm^{-3}, about 1 to 3 orders of magnitude lower than that in the experimental samples. This difference is attributed to the longer crystal growth time and crystal intergrowths in scoria.

4.2.2 Bubble number density, bubble shape, size, distribution, and permeability

The bubble number density (*BND*, i.e., the number of bubbles per unit volume of melt), is affected by the presence of crystals (Table 4.2). The *BND* is higher in both crystal-bearing experimental samples and in scoria than in aphyric or low-crystallinity samples in the same porosity range. The *BND* in natural scoria is from 1 810 to 3 611 vesicles mm^{-3} in the porosity range from 34 to 49%. In the crystal-rich experimental samples, the *BND* varies from 2 279 to 65 076 bubbles mm^{-3} in the porosity range from 31.6 to 55.3%. Particularly in the samples using starting material Bt17, which has high ϕ_{cry} of 48.3%, and has a very high population of crystals of 10^{-6} to 10^{-4} mm^3 in volumes, the *BND* can reach 25 960 to 65 076 bubbles mm^{-3}. The *BND* of samples from the same crystal-bearing

starting material tends to decrease with increasing vesiculation. In the crystal-free samples or samples with ϕ_{cry} below 10%, the *BND* is significantly lower, varying from 147 to 4 248 bubbles mm^{-3} (Bai et al., 2008).

Most bubbles are attached to crystals; some crystals are surrounded by bubbles, implying heterogeneous bubble nucleation and growth. Bubbles in samples dominated by small crystals of 10^{-6}–10^{-3} mm^3 are spherical (Figures 4.5a, 4.5b, and 4.7a), but bubbles are deformed and elongated in samples dominated by larger crystals of 10^{-4}–10^{-1} mm^3 (Figures 4.5c and 4.7b). Bubbles in samples with smaller crystals easily grow into sub-spherical to spherical bubbles of 1.4–1.9 mm^3 (Figures 4.5a, 4.5b, and 4.7c). 3-D tomographic images show that these large bubbles are connected to neighboring bubbles, not isolated in the melts. In contrast, the *BND* in natural scoria is 157–3611 mm^{-3} at porosities of 13–49.6%, lower than that in the experimental samples.

The bubble size distributions in crystal-bearing experimental samples follow power-laws, with exponents from 0.6 to 0.82 in the porosity range from 34 to 55.3% (Figures 4.8a and 4.8b). Most vesicle size distributions in scoria also display power-laws, but produce exponents of ~ 1.0 in the porosity range from 13 to 48.4% (Figures 4.8c and 4.8d). This is in agreement with the results found in Stromboli scoria from normal activity (Polacci et al., 2009).

Our comparisons amongst crystal-free and crystal-bearing samples demonstrate that crystals significantly influence bubble shape, size, distribution, and permeability. The permeabilities in crystal-bearing experiments and natural, crystal-rich scoria from Stromboli are about 1 to 2 orders of magnitude higher than those in aphyric experiments and natural, crystal-poor pumices in this porosity range (see discussion in section 5.6).

Figure 4.1 Permeability k and total porosity ϕ relationships for crystal-free samples from lattice-Boltzmann simulations and measurements (**a**) and permeability and porosity of relationships at porosities above 29%, the percolation threshold (**b**). The permeabilities from LB simulations and measurements are Darcian permeabilities. The standard deviations of uncertainties in LB simulations and measurements are indicated by the error bars for each point in (**a**) (Figure reproduced from Bai et al., 2010, *Journal of Geophysical Research* by permission of the American Geophysical Union).

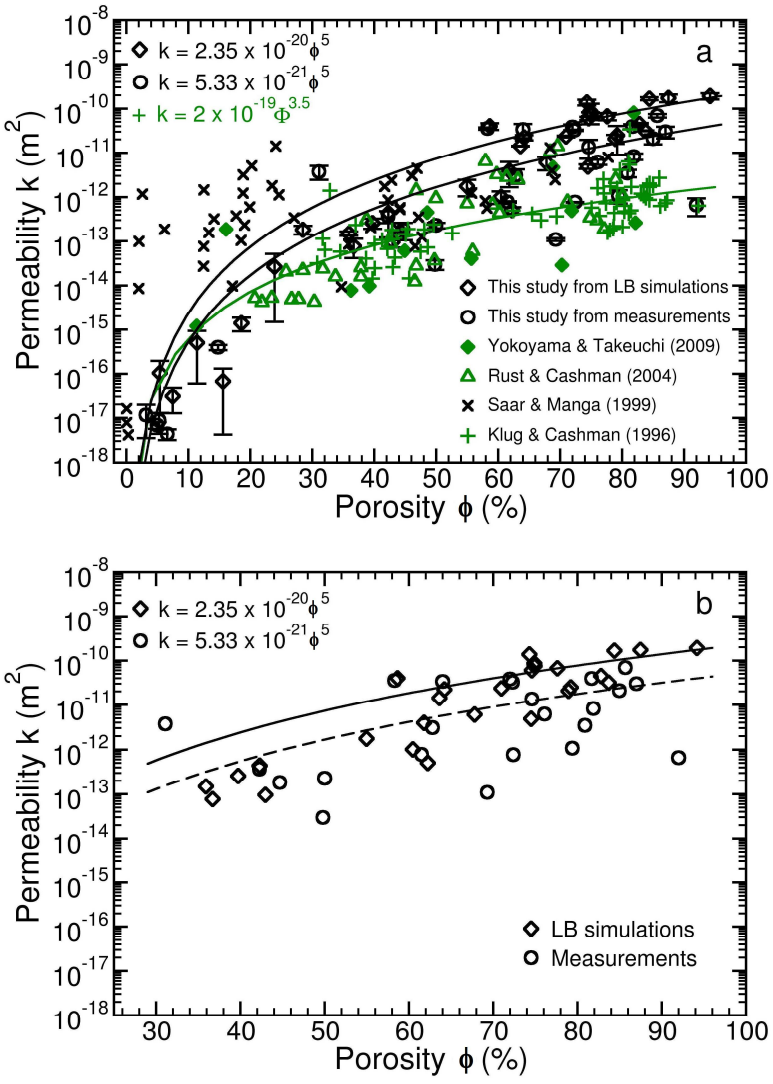

Figure 4.2 Scanning electron microscope images of samples St66b with a porosity of 46.3% (**a**) and St58a with a porosity of 66.7% (**b**). The holes in the bubbles (dark in color) are the interconnections or pore throats, which connect neighbouring bubbles (Figure reproduced from Bai et al., 2010, *Journal of Geophysical Research* by permission of the American Geophysical Union).

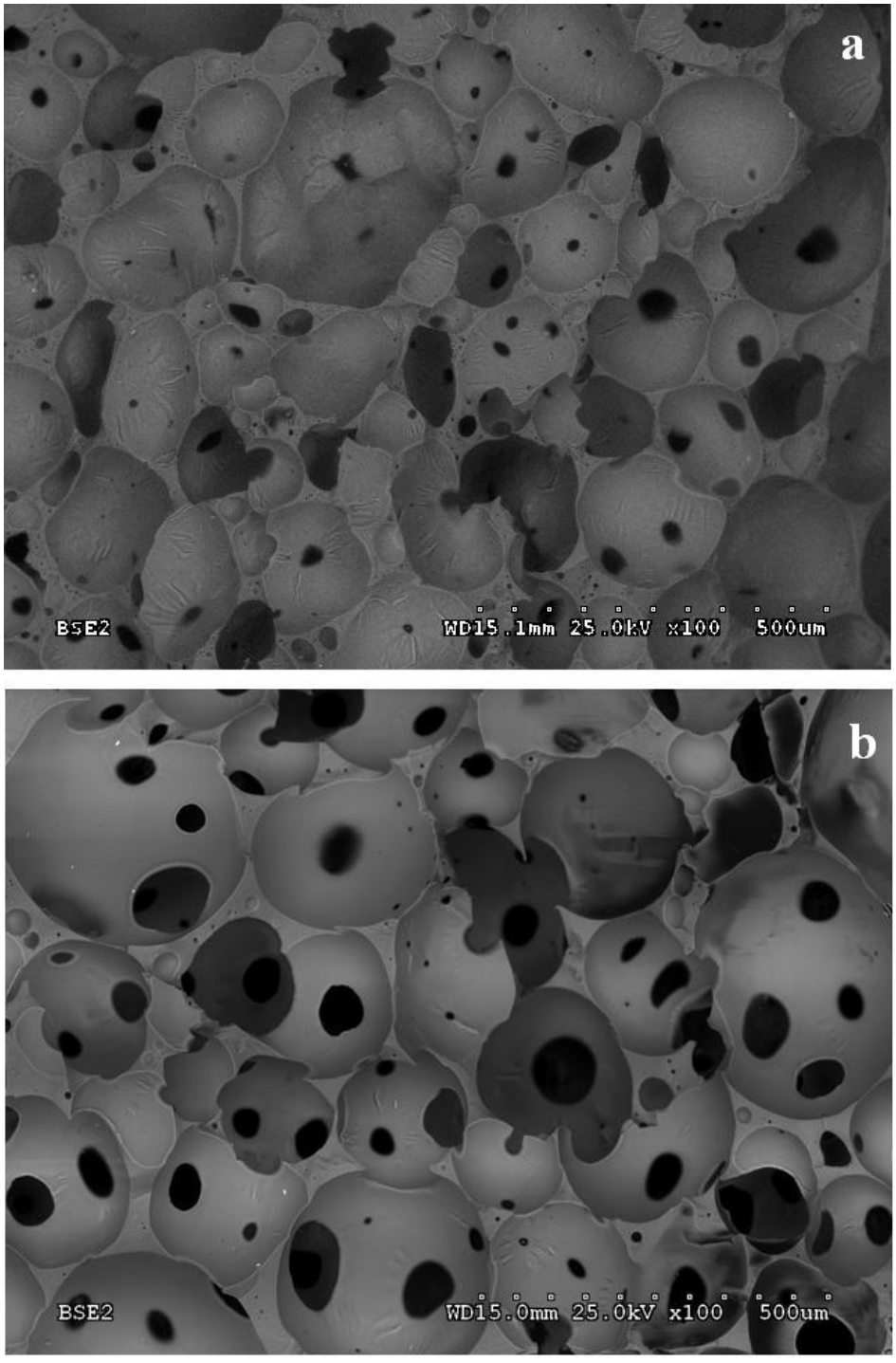

Figure 4.3 a: Experimental data of $\frac{P_i^2 - P_o^2}{2PL}$ vs u_g for selected samples; **b**: Experimental data of $\frac{P_i^2 - P_o^2}{2PLu_g^2}$ vs u_g for selected samples (Figure reproduced from Bai et al., 2010, *Journal of Geophysical Research* by permission of the American Geophysical Union).

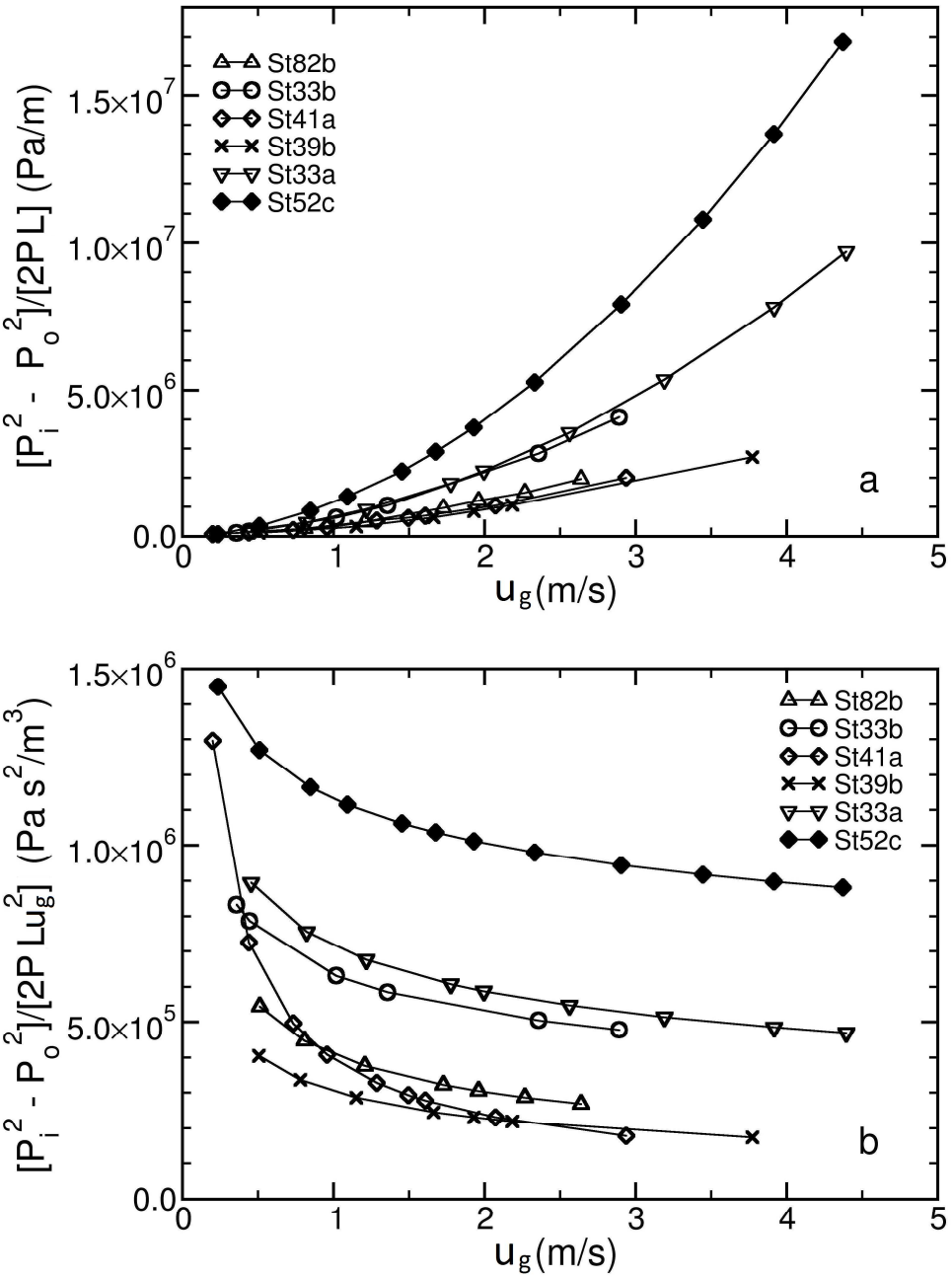

Figure 4.4 a: Relationships between Darcian permeability k_1 and non-Darcian permeability k_2; **b**: Correlation between Darcian permeability k_1 and bubble diameter D (μm); **c**: Correlation between non-Darcian permeability k_2 and bubble diameter D (μm). All are log-log plots (Figure reproduced from Bai et al., 2010, *Journal of Geophysical Research* by permission of the American Geophysical Union).

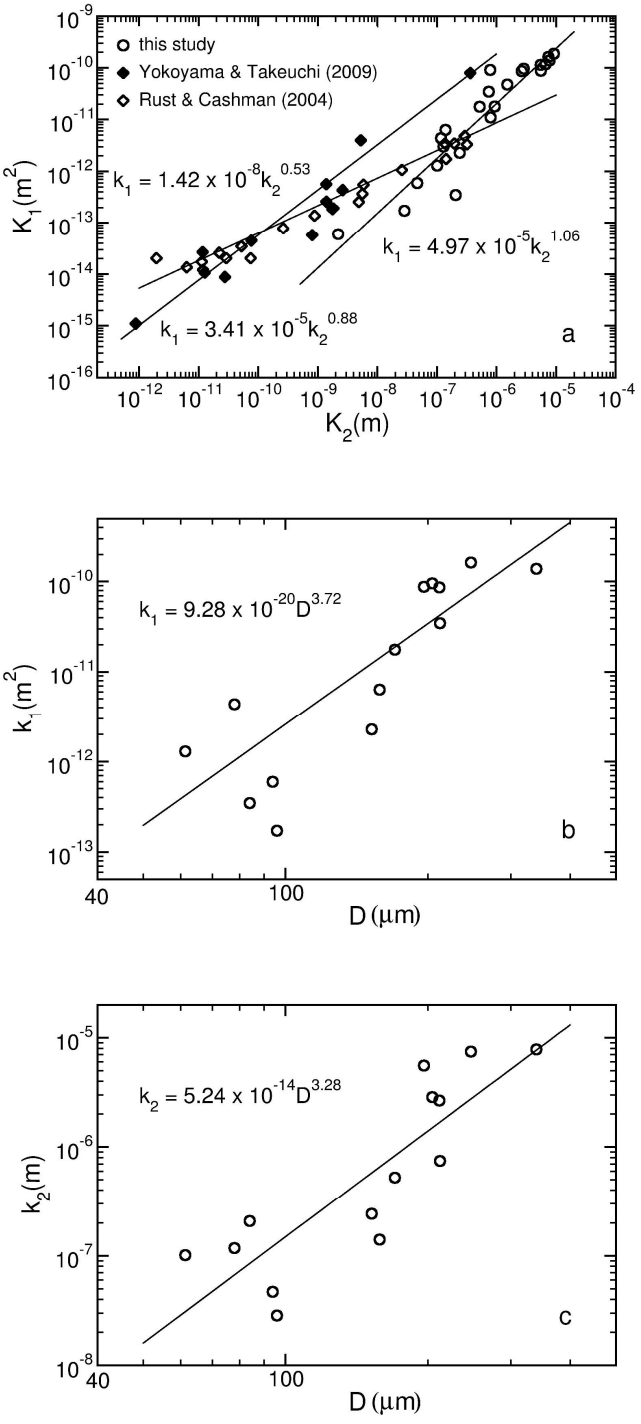

Figure 4.5 Backscattered electron images of crystal- and bubble-bearing samples Bt1a(**a**), SC23a(**b**), Bt7R(**c**), and Bt27(**d**). plg = plagioclase, cpx = clinopyroxene, gl = glass, spl = spinel. The plg has a skeletal shape in Bt1a, and the broken crystals are indicated by the cracks (black color) in Bt27 (Figures 4.5a and 4.5c reproduced from Bai et al., 2011, *Geophysical Research* Letters by permission of the American Geophysical Union).

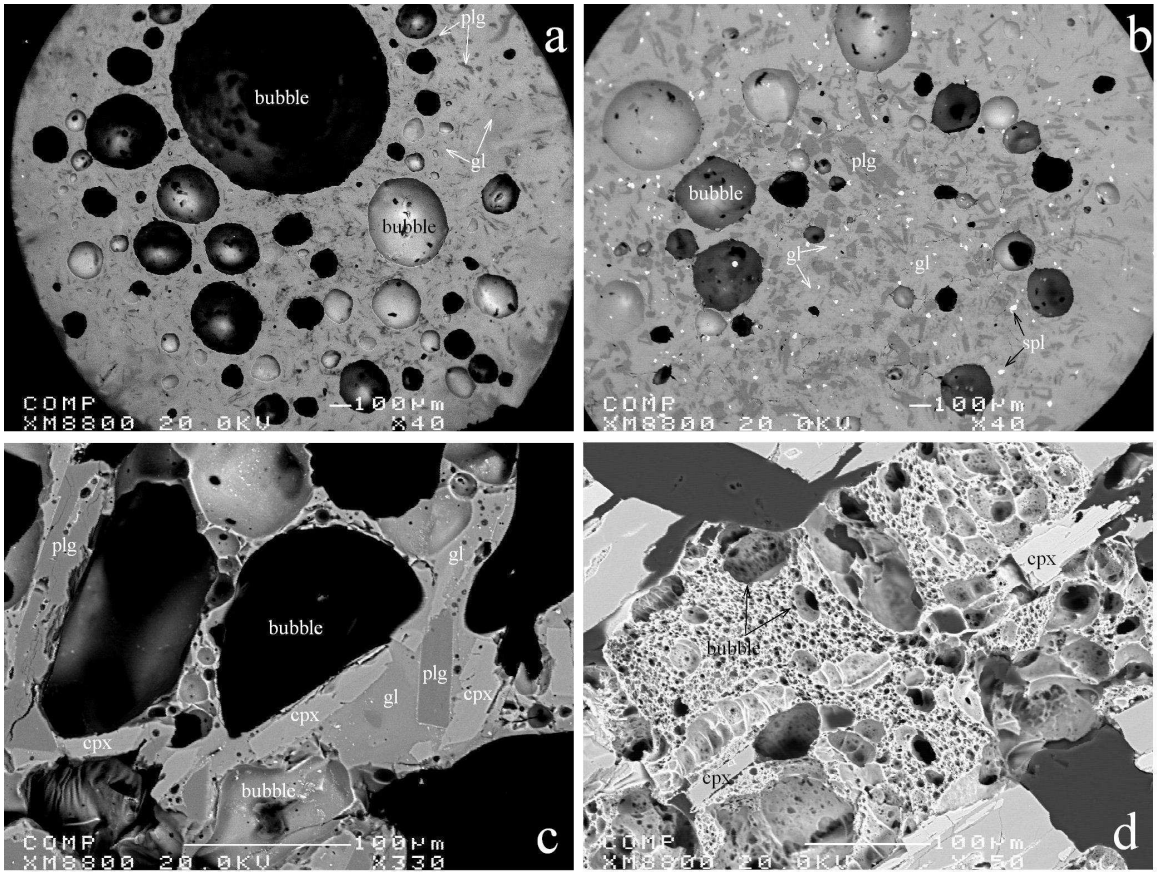

Figure 4.6 3-D cumulative (open circles) and non-cumulative (bars) crystal size distributions from tomographic images of experimental crystal-bearing Stromboli basalt samples Bt7R(**a**) and SC23a(**b**), and natural scoria from Stromboli Str240506b_b3(**c**) and Str250506_c2(**d**). r^2 is the correlation coefficient. The uncertainties in ϕ_{cry} are within 2 to 4.3% as discussed in section 2.2 (Figure 4.6d reproduced from Bai et al., 2011, *Geophysical Research Letters* by permission of the American Geophysical Union).

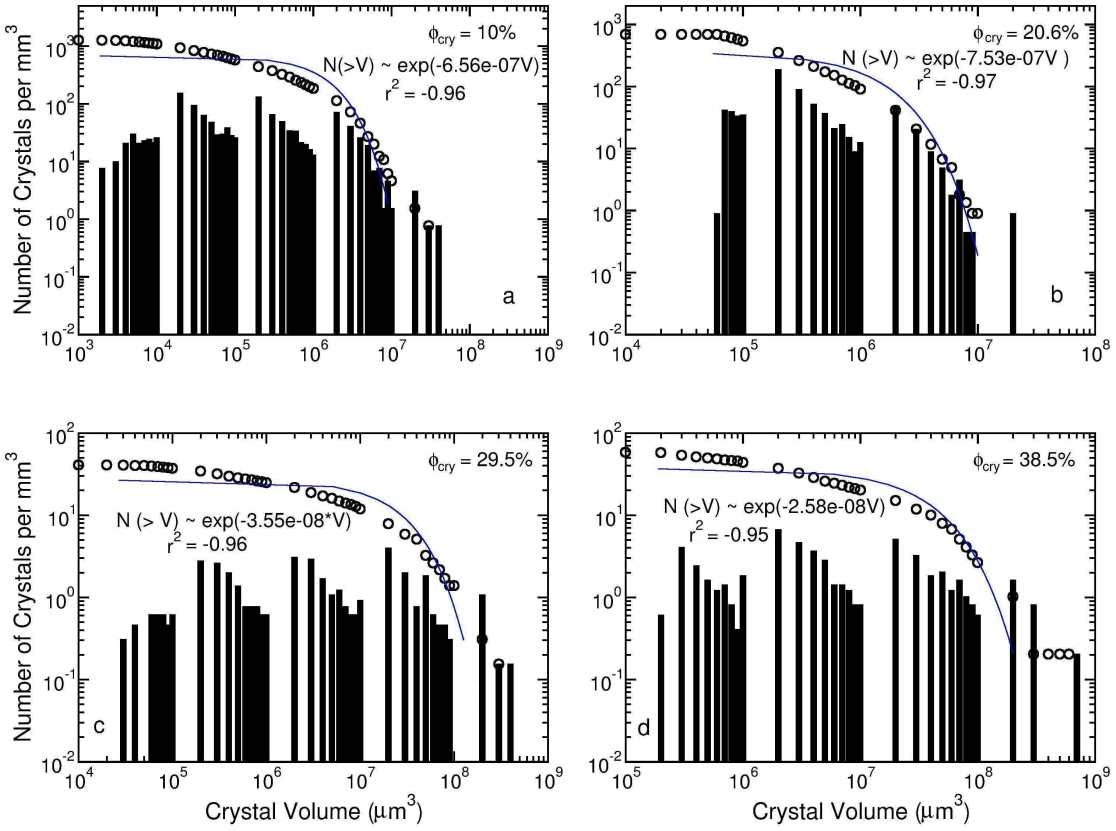

Figure 4.7 2-D slices from 3-D X-ray μCT of the degassed crystal-bearing samples Bt1b(**a**), Bt7c(**b**), SC23c(**c**), Bt22a(**d**). The scale bar is 300 µm (Figures 4.7c and 4.7d reproduced from Bai et al., 2011, *Geophysical Research Letters* by permission of the American Geophysical Union).

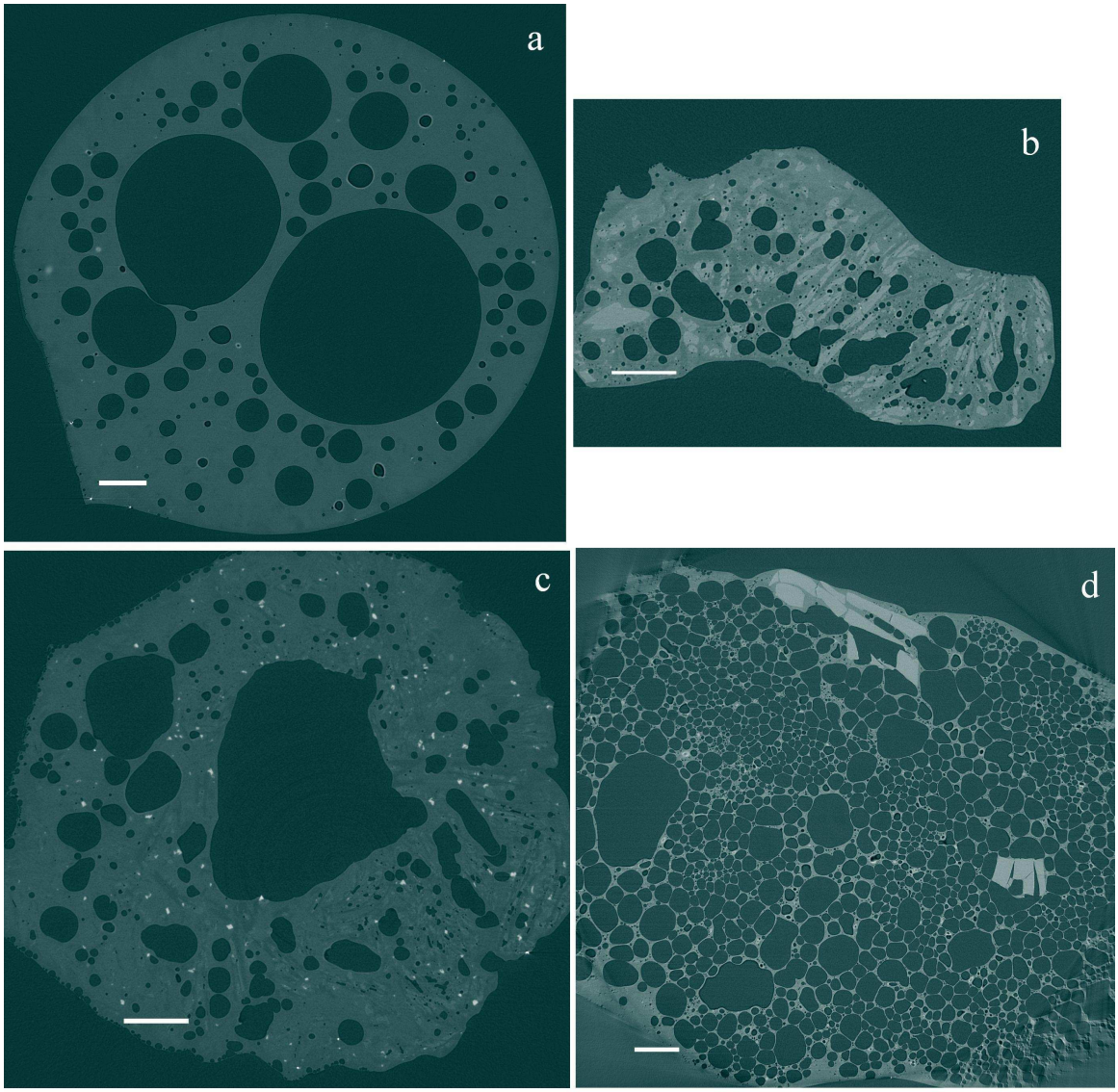

Figure 4.8 3-D cumulative (open circles) and non-cumulative (bars) bubble size distributions in experimentally produced, crystal-bearing, degassed Stromboli basalt samples Bt1c(**a**) and SC23c(**b**), and natural Stromboli scoria Str240506b_b3(**c**) and Str250506_c2(**d**). r^2 is the correlation coefficient. Bubble size distributions in crystal-free experiments performed on the same composition are found in Bai et al. (2008). The uncertainties in ϕ are within 3.1 to 5.0 % as discussed in section 2.2 (Figure 4.8d reproduced from Bai et al., 2011, *Geophysical Research Letters* by permission of the American Geophysical Union).

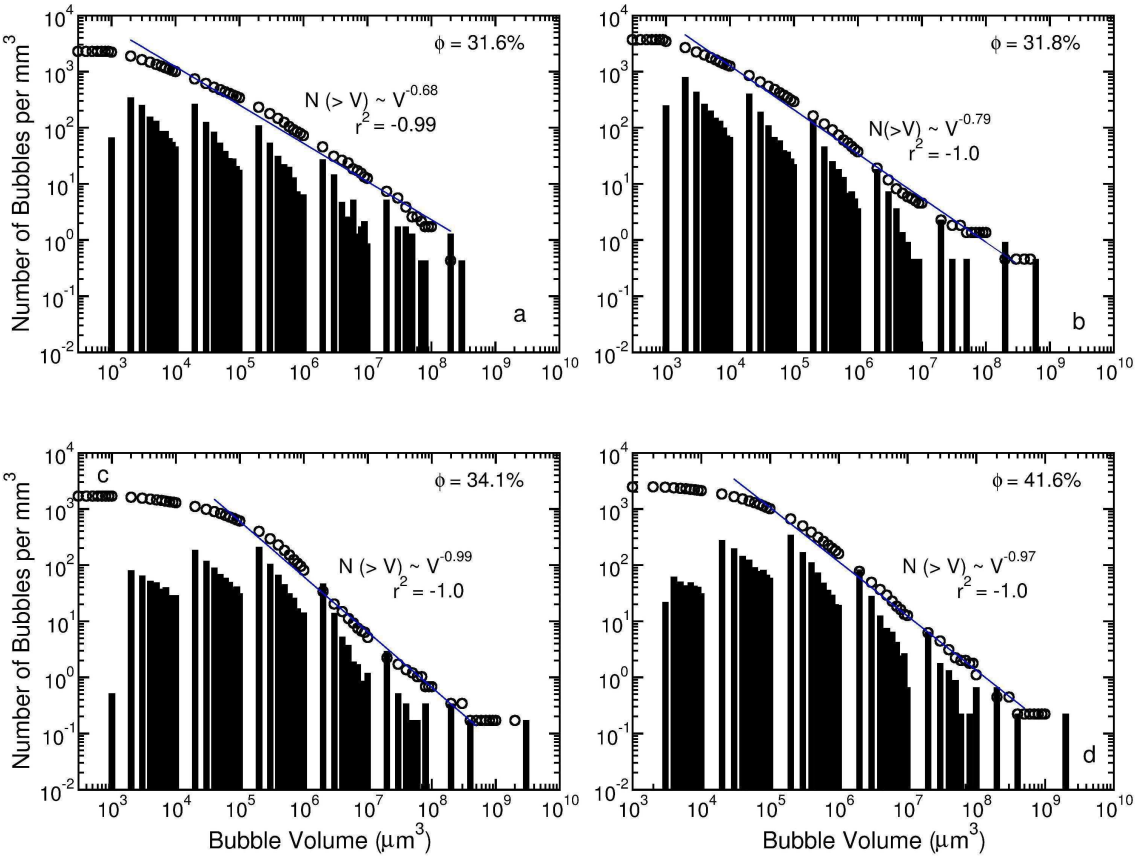

Table 4.1 Description of crystal-free samples and permeability results[a]

Sample	ϕ (%)	D (μm)	Distribution	$N_L a$ (μm)	Calculated k[b] (m^2)	Measured k[c] (m^2)	k_1 (m^2)	k_2 (m)	k_1/k_2 (mm)
St27	3.2	32.0	Exponential			1.16E-17			
St82	5.0	35.4	Exponential			6.81E-18			
St79	5.3	38.0	Exponential	970	3.09E-17	8.68E-18			
St61	6.6	34.8	Exponential	952	1.05E-16	4.34E-18			
St25	14.8	40.6	Exponential	952	6.8E-17	4.35E-16			
St7a	31.1		Power-law			2.36E-12	1.09E-11	7.99E-07	1.37E-02
St46a	39.7	94.0	Exponential	1216.5	2.56E-13	2.27E-13	5.94E-13	4.68E-08	1.27E-02
St43a	42.3	61.4	Power-law	980	4.36E-13	3.66E-13	1.29E-12	1.01E-07	1.27E-02
St41b	44.7	84.0	Power-law	840	9.58E-14	1.96E-13	3.46E-13	2.07E-07	1.68E-03
St43b	49.8		Power-law	1135.4	5.0E-13	2.97E-14	5.95E-14	2.21E-09	2.69E-02
St82b	58.3		Power-law	1443.6	1.75E-12	3.52E-11	1.13E-10	5.49E-06	2.06E-02
St41a	64.2		Power-law	1297.6	2.21E-11	3.85E-11	1.16E-10	6.66E-06	1.74E-02
St39a	61.5	78.0	Power-law	1120	1.01E-12	7.70E-13	4.34E-12	1.17E-07	3.70E-02
St73c	62.8		Power-law			3.09E-12	1.79E-11	9.37E-07	1.91E-02
St84f	72.0		Power-law	1164	1.37E-10	3.80E-11	9.06E-11	7.88E-07	1.15E-01
St7c	72.3		Power-law			3.21E-11	1.86E-10	9.15E-06	2.03E-02
St84ab	72.4	152.2	Exponential	970	6.02E-11	7.60E-13	2.27E-12	2.42E-07	9.37E-03
St29a	74.5	96.0	Exponential	1190	4.88E-12	1.09E-13	1.72E-13	2.84E-08	6.05E-03
St33a	74.6	211.7	Exponential			1.34E-11	8.60E-11	2.66E-06	3.23E-02
St87	76.1	212.4	Power-law			6.13E-12	3.46E-11	7.43E-07	4.66E-02
St46b	79.4	158.2	Exponential	1459.8	2.07E-11	1.07E-12	6.33E-12	1.40E-07	4.53E-02
St52a	80.9	170.4	Exponential	1622	4.44E-11	3.43E-12	1.76E-11	5.22E-07	3.37E-02
St39b	81.7	339.5	Exponential			3.91E-11	1.38E-10	7.80E-06	1.78E-02
St52c	81.9		Power-law	1332	3.14E-11	8.24E-12	4.74E-11	1.52E-06	3.11E-02
St33b	85.0	204.5	Exponential	1622	2.47E-11	2.08E-11	9.53E-11	2.86E-06	3.33E-02
St23b	85.7	246.9	Power-law	1951.2	7.49E-11	6.89E-11	1.62E-10	7.44E-06	2.18E-02
St25a	87.0	196.4	Exponential	1622	1.73E-10	3.08E-11	8.73E-11	5.56E-06	1.57E-02
St47b	92.4		Exponential	1480	1.91E-10	8.78E-13	3.02E-12	1.29E-07	2.35E-02
St84d	2.9		Power-law	485	5.02E-16				
St58b	18.5		Power-law	970	1.39E-15				
St52b	23.9		Power-law	1135.4	2.66E-14				

St26	25.6	Exponential	952	1.31E-14
St23a	35.9	Power-law	2168	1.49E-13
St37c	29.8	Power-law	1260	7.77E-14
St37a	52.5	Power-law	1050	3.96E-11
St69a	61.8	Power-law	1260	3.93E-12
St73a	61.9	Power-law	1184	6.02E-12
St64b	64.5	Exponential	776	1.42E-11
St65a	65	Exponential	970	2.33E-11
St58a	66.7	Exponential	970	8.6E-11
St84c	82.3	Exponential	970	3.18E-10
St58d	83.1	Exponential	776	6.63E-11

[a]Parameters are ϕ, porosity of entire sample determined by X-ray μCT (Our LB simulations used the subvolumes of the tomographic images of entire samples, see text for details); D, mean diameter of bubbles in samples, see text for details of D determination; $N_L a$, simulation sample sizes determined by lattice number N_L (voxels) along each edge multiplied by the grid resolution a (μm).

[b]Calculated Darcian permeability from LB simulations.

[c]Measured Darcian permeability.

Table 4.2 Description of crystal-bearing samples and permeability results from degassing experiments[c]

Sample	ϕ (%)	ϕ_{cry} (%)	*BND* (mm^{-3})	*CND* (mm^{-3})	$N_L a$ (μm)	[a]k (m^2)	[b]k (m^2)
Bt1a	36.1	31.7	2979		1310.4	(8.31±14.0)E-12	
Bt1b	42.7	16.1	405		873.6	(4.49±7.65)E-11	
Bt1c	31.6	16.1	2280				
Bt5b	52.8	19.0	18869	2951	655.2	(5.21±3.47)E-12	
Bt7b	67.4	20.0	4440		1562	5.66E-11	8.73E-14
Bt7c	34.3	34.5	13647	3547	1249.6	(2.97±3.51)E-12	
Bt7R	77.6	10		1076			
Bt27	62	36		3345	1270.8	(1.88±0.56)E-11	
SC23a	33.8	20.6	400	743	1310.4	(1.50±1.30)E-11	
SC23b	34.6	17.4	1506				4.7E-12
SC23c	31.8	20.5	3686	1020	1146.6	1.58E-10	2.1E-11
Bt17a	67.5	<10	1754		1146.6	1.59E-11	3.38E-11
Bt17c	55.3	19.1	25960		1146.6	(2.57±2.03)E-12	
Bt17d	54.7	17.1	65076				
Bt20	90.3	<5	3091		1874.4	6.54E-10	9.23E-11
Bt14	52.6	<5					1.2E-11
Bt22a	72.6	<5					
Str240506a	13	47.3	157	26	2160	(1.30±1.17)E-15	
Str240506b	47.3	35.7	3611	90	1890	(8.39±4.65)E-12	
Str150406b	44.5	33.0	169	38	2160	(4.05±0.29)E-11	
Str220506d	41.2	36.9	424	27	2160	(6.20±1.23)E-11	
Str240506b_b1	49.6	22.3	834	34			
Str240506b_b3	34.1	29.5	1627	74			
Str250506_c2	41.6	38.5	2517	51			

[c]Parameters are ϕ, porosity; $N_L a$, LB simulation sample sizes determined by lattice number N_L (voxels) along each edge multiplied by the grid resolution a (μm); [a]k, calculated Darcian permeability from LB simulations, the uncertainties are determined by

the standard deviations of permeabilities from LB simulations; ${}^{b}k$, measured Darcian permeability; a, grid resolution (a = 5.46 to 9 μm); ϕ_{cry}, *BND*, *CND* see text for details. Note that the last 7 samples are scoria from Stromboli, the others are experimental samples.

CHAPTER 5: DISCUSSION

5.1 Comparison lattice-Boltzmann permeabilities with other studies

Previous lattice-Boltzmann simulations indicated that sandstone permeabilities are in the range 10^{-13} to 10^{-11} m^2 at porosities below 30% and that the simulations agree with measured permeabilities (Bosl et al., 1998; Keehm et al., 2004; Arns et al., 2005; Fredich et al., 2006). These permeabilities are about 1 to 2 orders of magnitude higher than our simulations at similar porosities. Such differences might be caused by the different pore geometries in the sandstone and in our experimental samples, where in sandstone the porosity occurs between sub-spherical grains whereas in our samples the porosity is created by sub-spherical vesicles. We performed a test by comparing our lattice-Boltzmann simulations to sandstone permeabilities determined in earlier studies. To take into account the different geometries we inverted our images so the pores are considered solids to mimic the pore structure of sandstone. Lattice-Boltzmann simulations performed on these "inverted" tomographic images yielded permeabilites of 1.3×10^{-12} to 6.8×10^{-12} m^2 at porosities of 14.3 to 50.2%, in good agreement with sandstone permeabilities from simulations and measurements in that porosity range (Bosl et al., 1998; Keehm et al., 2004; Arns et al., 2005; Fredich et al., 2006).

5.2 Comparison between simulated and measured permeabilities of crystal-free experiments with volcanic rocks

Previous permeability measurements on natural basaltic rocks (Saar and Manga, 1999; Mueller et al., 2005) indicated that basalts can attain permeabilities 10^{-13} to 10^{-9} m^2 at porosities over ~ 30%, consistent with our results. However, calculated and measured permeabilities of crystal-free samples in our study are about 2 orders of magnitude higher than the permeabilities of rhyolitic and dacitic volcanic rocks with porosities over ~ 30% (Klug and Cashman, 1996; Rust and Cashman, 2004; Wright at al., 2009; Yokoyama and Takeuchi, 2009, and Figure 4.1).

One of the significant results in our permeability-porosity relationship is the transition at porosities of approximately 29 volume percent (Figure 4.1a). The permeability is low (10^{-17} to 10^{-14} m^2) at porosities below 29%; the permeability increases markedly in the porosity range 18.5 to 29% where the percolation threshold is approached, and permeabilities attain values of 10^{-10} to 10^{-9} m^2 at porosities over 65%. In our study, the permeability increases significantly at the threshold, because permeability development requires bubble-bubble coalescence and interaction during degassing creating a porous network that efficiently spans the sample.

The higher permeabilities are attributed to a higher degree of bubble interconnectivity and larger bubble apertures in our basaltic samples than in rhyolitic ones. In these samples, most bubbles are spherical and multiply connected at high porosities (Figure 4.2 and Bai et al., 2008). Klug et al. (2002) showed that most bubbles are elongated in one direction in one natural rhyolite, and that the bubbles connect with each other only along their edges; thus, bubble edges dominate the pore geometry and result in lower permeabilities than in this study.

The 3-D tomographic images of our samples show that bubble coalescence is extremely rare at porosities below 18.5%. With significant bubble coalescence, a percolation cluster appears to form at a porosity of about 29%. 3-D tomographic and SEM images of degassed samples indicated that bubble coalescence is common at porosities over 29%, where we observed partially coalesced bubbles composed of interpenetrating spheres and bubble walls that were thinned and ruptured. At porosities over ~ 65%, a foam formed by multiply connected, coalesced bubbles, and the degree of bubble connectivity is extensive (Figure 4.2 and Bai et al., 2008). The coalesced bubble aperture diameters can attain ~ 40 to 70 μm in the porosity range 40% to 65% and ~ 110 to 140 μm in the porosity range 72% to 92.4% due to coalescence. We estimated the bubble connectivity of our samples by (Okumura et al., 2008):

$$Connectivity = \frac{V_{\max}}{V_{bubble}} \tag{5.1}$$

where V_{max} is the volume of the largest bubble, and V_{bubble} is the total bubble volume. Estimated connectivities are in a range of 0.74 to 0.96 at porosities over ~ 65%, implying a high degree of interconnected porosity, and therefore a high permeability. This high degree of connectivity results from bubble coalescence in the low viscosity basaltic melts studied, ~ 50 Pa s (Giordano and Dingwell, 2003). On the contrary, rhyolitic and dacitic volcanic rocks have high viscosities, which inhibits bubble coalescence and restricts the bubble interconnectivity, producing bubble aperture diameters of only ~ 2 to 10 μm in the porosity range 78 to 85% (Klug et al., 2002). Previous experimental studies on bubble apertures show that Darcian permeability, *k*, is strongly correlated with pore aperture diameter; larger aperture sizes produce higher permeabilities (Klug et al., 2002; Yokoyama and Takeuchi, 2009).

5.3 Bubble size and distribution effects on k_1 and k_2 in crystal-free experiments

As is evident from Table 4.1 and Figures 4.4b and 4.4c, the permeability constants k_1 and k_2 are sensitive to bubble sizes and distributions. Generally, k_1 and k_2 in samples with power-law bubble size distributions are higher than for samples with exponential bubble size distributions. This is more obvious in samples St7c, St7a, St41a, St52c, St82b, and the natural sample, which are different from samples of St29a, St84b, St46a, St47b with exponential bubble size distributions. 3-D tomographic images and 3-D bubble size distributions show that bubble sizes vary by ~ 2 to 4 orders of magnitude in samples with power-law bubble size distributions; a few bubbles can be up to 200 to 300 μm in diameter and are generally surrounded by medium and small bubbles (Figures 5.1b and 5.1c). The types of bubble sizes and distributions in these samples are consistent with observations on natural scoria from normal Strombolian activity (Polacci et al., 2009). Bubbles in samples with exponential distributions tend to be of medium size, ~ 96 to 152 μm in diameter, although these samples have higher total porosities of about 72 to 92% (Figure 5.1d). Plots of k_1 or k_2 versus bubble diameter *D* (μm) in our study reveal a strong correlation between k_1, k_2 and bubble size *D* (Figures 4.4b and 4.4c); k_1 and k_2 increase

with *D*. Walsh and Saar (2008) simulated a single-phase assembly of large bubbles, and added a second small-bubble population to the void space, demonstrating that the small-bubble population did not contribute significantly to the overall permeability, although the small-bubble population might increase bubble connectivity.

Because permeability is sensitive to porosity and pore structure, it is necessary to quantitatively describe the pore size and porosity effect on the permeability. For monodisperse spherical particles, the relationship between permeability and pore size and porosity is well expressed by the semi-empirical Ergun equation (Ergun, 1952; Sidiropoulou et al., 2007):

$$k_1 = c_1 \frac{D^2\phi^3}{(1-\phi)^2} \tag{5.2}$$

$$k_2 = c_2 \frac{D\phi^3}{1-\phi} \tag{5.3}$$

where c_1 and c_2 are constants, D is the pore or bubble diameter, and ϕ is the porosity. We evaluated the above equations based on our measured permeabilities. Note that we did not include the data sets St7a, St7c, St41a, St43b, St52c, St73c, St82b, and St84f (natural sample) because these samples have obvious power-law bubble size distributions, and an average bubble diameter cannot be defined accurately. Sample St47b was also not used because it has a porosity of 92.4% and most bubbles are highly connected, so we could not separate the bubbles in the foam into individual bubbles and measure their diameters using Blob3D.

Fitting k_1 against $\frac{D^2\phi^3}{(1-\phi)^2}$ and k_2 against $\frac{D\phi^3}{1-\phi}$ furnishes $k_1 = 7.66\times10^{-17}\frac{D^2\phi^3}{(1-\phi)^2}$ and $k_2 = 2.78\times10^{-9}\frac{D\phi^3}{1-\phi}$ (Figures 5.2a and 5.2b), demonstrating the relationships given by equations (5.2) and (5.3). The significant dispersion of k_1 and k_2 about the best-fit lines might be explained by the effect of the geometrical factors. In this study, we define a

geometrical factor $\alpha = \frac{\sqrt{k_1}}{k_2}$, which is a dimensionless function of the pore geometry. The values of α vary from 1.6 to 18 in the porosity range of 31% to 92.4%; α tends to be higher for the samples with power-law bubble size distributions. For samples with a porosity below ~ 65%, the degree of bubble coalescence is low and the coalesced bubbles are randomly distributed, so the spatial arrangement of bubbles and the tortuosity of the flow can vary significantly between samples; thus, the geometry factor α and permeability are expected to be more sensitive to the pore structure. For the samples with porosities ~ 65% and greater, most bubbles are connected to form a foam, and the spatial arrangement of bubbles tends to be homogenous; accordingly, the influence of the geometry factor on permeability tends to decrease. The relationship between α and bubble size (Figure 5.2c) demonstrates that α decreases with increasing bubble size (which is positively correlated with porosity). Thus, α might have a larger influence on the permeability of samples with small bubble sizes (low porosity); this results in the significant dispersion in small bubble size ranges shown in Figures 5.2a and 5.2b. At high porosity, ~ 65% to 92%, bubble sizes are larger, the geometry factor tends to be a constant, and permeabilities k_1 and k_2 have a stronger dependence on bubble size and porosity. Our results quantitatively constrain the relation between pore sizes, porosity and permeability. **A**s shown above, the occurrences of k_1 and k_2 strongly depend on the flow velocity and pore geometry, if we can determine the variation of flow velocity and pore geometry in the vesicular magma, we can expect to determine whether Darcian permeability or Non-Darcian permeability dominates the flow in the vesicular magma. However, because our samples are from degassing experiments with spherical bubbles, we cannot estimate the effects of other factors on the permeability, including tortuosity and pore shape. Bubble diameters in natural Stromboli basaltic pumice and scoria can be up to 0.5 to 4 mm (Polacci et al., 2008, 2009), and bubbles are elongated. In this case, tortuosity and pore shape influences on the permeability are expected to be significant, and future studies are needed to incorporate tortuosity and pore shape effects on permeability.

5.4 Correlation between friction factor f_k and Forchheimer number *Fo* in crystal-free experiments

The experimental data plotted in Figure 4.3b show the transition from Darcian flow to Forchheimer flow due to the increasing inertial contributions. However, Figure 4.3b can not clearly delineate the regimes of Darcian flow and non-Darcian flow. The presence of inertial effects, particularly the transition to turbulent flow is highly dependent on pore geometry (Wood, 2007). To clearly delineate the transition between Darcian flow, non-Darcian flow, and turbulent flow, we write the Forchheimer equation as:

$$(\frac{P_i^2 - P_o^2}{2PL})\frac{k_2}{\rho_l u_l^2} = 1 + \frac{1}{Fo} \tag{5.4}$$

where the left-hand side of equation (5.4) is the friction factor f_k for fluid flow in porous media (Holdich, 2002), $f_k = (\frac{P_i^2 - P_o^2}{2PL})\frac{k_2}{\rho_l u_l^2}$. f_k describes the friction of fluid flowing over the porous media surface that causes a pressure drop, and relates the shear stress at the surface of the solid to the pressure gradient.

Equation (5.4) shows that f_k tends to a constant value of 1 when $Fo >> 1$. In this case, f_k is independent of *Fo* for fluids when $Fo >> 1$, and it is only dependent on k_2, which itself is pore size and structure dependent. Given a velocity u_l, a Forchheimer number, *Fo*, a pressure gradient $(\frac{\Delta P}{L})$ and a density ρ_l, we can determine f_k for gas flow in porous media. The results of friction factor-Forchheimer number correlations (f_k – *Fo*) obtained from the measurement data of the selected crystal-free samples are shown in Figure 5.3a. *Fo* and f_k from the other measurements of samples fall on the same trend line shown in Figure 5.3a. Generally, f_k decreases with increasing *Fo* with a linear relationship when $Fo << 1$, corresponding to Darcian flow. As *Fo* increases, the inertial effects are increasingly significant and the transition from Darcian flow to non-Darcian flow occurs. The transition occurs when *Fo* is in the range ~ 0.2 to 10, as indicated by the gradual departure from linearity in Figure 5.3a. The *Fo* range where the transition occurs is consistent with

previous simulations and experiments (Venkataraman and Rao, 1998; Andrade et al., 1999). Consistent with the definition of f_k, it reduces to a constant of 1 when $Fo >> 1$. The occurrence of a transition region implies a gradual change from Darcian to non-Darcian flow, rather than an abrupt change. This behaviour was previously suggested to be a common phenomenon for fluid flow through spherical pores (Venkataraman and Rao, 1998).

To compare simulations with measurements, we performed lattice-Boltzmann simulations of flow with increasing body forces $\boldsymbol{f} = 1.0 \times 10^{-6}$, 1.0×10^{3}, 5.0×10^{3}, 1.0×10^{4}, 5.0×10^{4}, 1.0×10^{5}, where the uniform pressure gradient is equal to the force $\boldsymbol{f}$ per unit volume, i.e., $\langle \nabla P \rangle = \frac{f}{V}$. Here, V is the nondimensional volume of a simulation sample ($V = N_L^{\,3}$). Accordingly, the Forchheimer equation for the lattice-Boltzmann fluid can be written as:

$$\langle \nabla P \rangle = \frac{\mu_l}{\ell^2} \langle u \rangle + \frac{\rho_l}{k_2} \langle u \rangle^2 \tag{5.5}$$

where ℓ is Brinkman screening length, $\ell^2 = k_1$, ρ_l is the lattice-Boltzmann fluid density which is a nondimensional parameter (ρ_l = 24 in our simulations), μ_l is the lattice-Boltzmann fluid viscosity (μ_l = 0.24), and $\langle u \rangle$ is the velocity. We scale the uniform pressure gradient $\langle \nabla P \rangle$ with $\frac{\langle u \rangle^2 \rho_l}{\ell}$ to calculate the friction factor f_k, then equation (5.5) can be rearranged in the form:

$$\frac{\langle \nabla P \rangle \ell}{\langle u \rangle^2 \rho_l} = \frac{1}{Fo} + \frac{\ell}{k_2} \tag{5.6}$$

We define $f_k = \frac{\langle \nabla P \rangle \ell}{\langle u \rangle^2 \rho_l}$, and $Fo = \frac{\rho_l \langle u \rangle}{\mu_l} \ell$. In this case, *Fo* in the simulations is analogous to *Fo* in the experiments ($Fo = \frac{\rho_l u_l}{\mu_l} \left[\frac{k_1}{k_2} \right]$) as discussed in section 2.2, both $\frac{k_1}{k_2}$ and ℓ have the dimensions of length. Note that the characteristic length of *Fo* in simulations is different from that in measurements, because *Fo* in the simulations is constrained by the nondimensional parameters of velocity $\langle u \rangle$, ρ_l, and ℓ. The results of the LB simulations in terms of friction factor f_k and *Fo* for different sample porosities are shown in Figure 5.3b. The simulations agree with the experimental results and display a transition from Darcian flow to non-Darcian flow. The departure from linearity occurs in the *Fo* range ~ 0.2 to 1 for most samples with porosities over ~ 75%, and in the range of 1 to 10 for samples with porosities below ~ 75%, consistent with the experimental observations. We fit the results of measurements and simulations to constrain the relationship between the friction factor f_k and *Fo*: $f_k = (1.11 \pm 0.17) + \frac{0.66 \pm 0.39}{Fo}$ (for measurements), $f_k = (0.59 \pm 0.49) + \frac{1.0 \pm 0.01}{Fo}$ (for LB simulations). The fit to the measurement is close to that of the simulations if the uncertainties in the fitting are considered.

In our studies for samples with higher k_2 values, the manifestation of the inertial effect tends to occur at low *Fo* values for samples with a higher geometry factor α. Samples St46b, St47b, and St46a, which display the inertial effect in the *Fo* range of 0.2 to 1 (Figure 5.3a), have high α values of 13.5 to 18, in comparison with St52a, with lower α value of 8, that displays the inertial effect in the *Fo* range of 8 to 10. The manifestation of the inertial effect also tends to occur at small *Fo* values for samples with relatively higher geometry factors in our simulations. This observation in both the measurements and the simulations demonstrates that inertial effects are highly dependent on pore geometry.

The occurrence of turbulent flow at *Fo* values between 0.1 and 10 was not identified in either our experimental measurements or LB simulations. Wood (2007) suggested that the transition to turbulence varies with the pore geometry, and that fully turbulent flow

regimes occur when $Fo > 300$. Our results show a gradual transition regime of Darcian to non-Darcian flow with Fo in the range 0.1 to 10. This suggests that the transition from Darcian to non-Darcian flow is gradual (Venkataraman and Rao, 1998). In this transition, the friction factor f_k depends on both k_2 and Fo, and both the inertial and viscous forces contribute to the dissipation. Beyond the transition, corresponding to $Fo >> 1$, f_k reduces to a constant, becoming a function only of k_2, which itself is a function of the pore structure. Therefore f_k depends on pore size, shape, and geometry at large Fo, i.e., at conditions of turbulent flow.

Note that our samples are from degassing experiments with bubble sizes in the range ~ 30 to 340 μm, and the bubbles tend to be fully penetrable spheres at porosities above ~ 65%. In contrast, bubble sizes in natural Stromboli basaltic magma can attain diameters in the range ~ 0.5 to 4 mm (Polacci et al., 2008, 2009) and ~ 0.4 to 1 mm in diameter in rhyolitic magmas close to the critical porosity for magma fragmentation (Wright et al., 2009); thus, k_2 might increase in the natural samples, with inertial effects dominating at large Fo. In this case, gas flow through porous media with large pore sizes and geometry factors is expected to be turbulent flow.

5.5 The effect of crystals on bubble growth, bubble size and distribution

Our results show that crystals influence bubble size and shape. In samples that primarily have smaller crystals of 10^{-6}–10^{-3} mm^3 and $\phi_{cry} > 16\%$, a large spherical to sub-spherical bubble is generally formed (Figures 4.7a and 4.7c); this is different from the behavior in samples with $\phi_{cry} < 10\%$ and in aphyric samples, where most bubbles connected to form a foam after similar growth durations (Figure 4.7d and Bai et al., 2008). The large bubbles in crystal-bearing experiments grow at the expense of small-to-medium sized bubbles, because *BNDs* decrease with bubble growth duration.

Previous studies show that Ostwald ripening can control the growth of larger bubbles at the expense of small bubbles (Lautze et al., 2011). The coarsening time τ for a bubble with radius r_b can be estimated by (Herd and Pinkerton, 1997):

$$\tau = \frac{r_b^2 P\delta}{4RTD_{H2O}\sigma S} \quad (5.7)$$

where δ is the melt film thickness separating two bubbles, R is the gas constant, T is absolute temperature, P is pressure, D_{H2O} is the water diffusion coefficient, S is the water solubility, σ is the surface tension. The ripening rates for bubbles show that when Ostwald ripening influences the bubble size distribution, $\tau \sim r_b^3$, and for ~ 10 μm bubbles, τ reaches 30 min in basaltic magma (Herd and Pinkerton, 1997) and 40 min in rhyolitic magma (Larsen et al. 2004). In our experiments, the bubble growth duration was only up to ~ 10 min, so Ostwald ripening can not account for the growth of the large bubbles. Instead, the large bubbles form by bubble expansion and coalescence. Crystals are tangentially aligned around the large bubbles (Figure 4.5a), indicating that the small-to-medium sized crystals are pushed and oriented by bubble expansion. Also, in the samples with larger crystals, bubbles grow on the surface of crystals, and the medium-to-large bubbles are trapped between the crystals. These bubbles are deformed and elongated due to bubble expansion around the crystals, and the coalesced bubble walls are highly ruptured (Figures 4.5c and 4.5d). These observations are direct indications that bubble expansion and coalescence cause the growth of large bubbles.

Experimental crystal-bearing run products produce power-law bubble size distributions with exponents ranging from 0.6 to 0.82 in the porosity range of 13 to 55.3%; these exponents are lower than in crystal-free experimental samples in the same porosity range, ~ 1 to 1.42 (Bai et al., 2008 and Chapter 4). The smaller power-law exponents derived from our crystal-bearing samples imply fewer multiple bubble nucleation events, because the power-law exponent can be associated with the number of the nucleation events (Blower et al., 2001). Multiple bubble nucleation events are affected by the concentration of exsolved volatiles in the melts during degassing. The initial bulk volatile concentrations in our crystal-bearing glasses before degassing are mostly in the range from 2.4 to 3.6%, except for SC23, which has 6% H_2O. In contrast, initial volatile concentrations in our previous crystal-free glasses before degassing were 2.9 to 7.2% H_2O

or 2.9 to 7.2% H_2O + 440 to 1478 ppm CO_2 (Bai et al., 2008 and Chapter 2). The higher volatile concentrations in the crystal-free glasses might be more supersaturated during degassing, consequently producing a higher number of nucleation events. These results are supported by electron microprobe analysis of the degassed samples. The oxide totals are up to 99.4% in Bt1a and SC23a, which did not show multiple nucleation events, and the power-law exponent in the bubble size distribution is 0.6 to 0.79. This suggests that most volatiles in the glasses were depleted during early degassing; there are fewer volatiles left to exsolve from the melt to create multiple nucleation events with continued degassing. In contrast, the oxide totals in Bt5b and Bt17c are from to 95 to 95.6, suggesting that the volatiles in these two glasses were not totally depleted during degassing, therefore, more multiple nucleation events occurred, producing higher power-law exponents, from 0.77 to 0.82.

5.6 Permeability comparison between crystal-free, crystal bearing samples and natural scoria

The permeability-porosity data of the experimental crystal-bearing samples are fit with a Kozeny-Carman relation: $k(\phi) = 2.04 \times 10^{-20}\ \phi^{5.24}$ (Figure 5.4). Note that during LB simulations on crystal-bearing samples, we simulated fluid flow through binary 3-D porous samples (pore + solid), all bubbles were treated as pore phase, and all the crystals and melts were treated as solid phase. We can not simulate fluid flow through 3-D samples consisting of three different phases (pore + crystal + melt). The natural scoria yields permeabilities of 8.4×10^{-12} to 4×10^{-11} m^2 at porosities of 34.1–49.6%, consistent with the permeabilities of the experimental samples in the same porosity range. Scoria Str240506a, with a ϕ of only 13% and ϕ_{cry} of 47.3%, has a permeability of 10^{-15} m^2, similar to the permeability of crystal-free samples at the same porosity. The permeabilities in the crystal-bearing samples are ~ 10^{-12}–10^{-10} m^2 at porosities of 31.6–55.3%, about 1–2 orders of magnitude higher than those in aphyric samples in the same porosity range (Chapter 4). This result is consistent with Polacci et al. (2009), who demonstrated that the permeability of Strombolian scoria is about one order of magnitude higher than that of one pumice clast erupted during the April 2003 and another clast from

the March 2007 paroxysmal eruptions. The higher permeability is attributed to the effect of crystals on the bubble sizes and distributions discussed above.

Darcy permeability *k*, bubble size, and porosity ϕ can be related by the Ergun equation (Ergun, 1952):

$$k = c\frac{D^2\phi^3}{(1-\phi)^2} \tag{5.8}$$

where *c* is a constant, *D* is the pore (bubble) diameter. Permeabilities in samples with larger bubbles are higher than those in samples with medium-size bubbles (Chapter 2). In crystal-bearing samples, larger bubbles are generally present, resulting in higher permeabilities, as given by the Ergun equation; also, the coalesced bubble walls are highly ruptured, producing larger bubble apertures, and thus higher permeabilities.

At higher porosities, ~ 55.3 to 90%, the permeabilities of both crystal-bearing and crystal-free samples are similar. In this porosity range, ϕ_{cry} is below 10%, the crystals can not have a significant effect on bubble shape, size, distributions, and coalescence as indicated from 3-D tomographic images (Figure 4.7d and Bai et al., 2008), thus the crystal effect on the permeability is small.

The *BNDs* in the experimental samples are higher than those in natural scoria because our experiments are similar to the degassing conditions within a few seconds to minutes after formation and most probably prior to eruptions, where bubbles are not modified by syn- and posteruption processes. Scoria probably has undergone longer bubble growth durations, which can decrease the *BNDs* due to bubble coalescence. In experiments with longer bubble growth durations, Bt1b and SC23a, the *BNDs* decrease to values similar to those of the scoria. Our results show that bubble size distributions in the experimental samples follow a power-law, consistent with scoria (Polacci et al., 2009). However, the power-law exponents in scoria generally are near 1, higher than measured in experimental samples, ~ 0.6–0.82.

The power-law exponent has been associated with the number of the nucleation events (Blower et al., 2001). ϕ_{cry} in scoria are 22.3–47.3%, whereas ϕ_{cry} in the degassed experimental samples are only 16–34.5%. The high ϕ_{cry} in scoria might induce more multiple nucleation events during scoriaceous magma eruption because crystals can decrease the supersaturation required for bubble nucleation and facilitate bubble nucleation (Hurwitz and Navon, 1994).

Figure 5.1 3-D bubble size distributions from 3-D tomographic images of experimentally produced vesicular Stromboli basalt samples with different porosities. The colors distinguish independent bubbles. Blue represents the pore phase (bubble) and red represents the solid phase (glass). **a**: sample St26 with a porosity of 25.6%; **b**: sample 41a with a porosity of 64.2%; **c**: sample St52c with a porosity of 81.9%; **d**: sample 29a with a porosity of 74.5%. St26 and St 29a have an exponential bubble size distribution; St41a and St52c have a power-law bubble size distribution. The bars in the plots are the bubble size distributions indicated by log V (bubble volume) ~ log N (bubble number), the open circles and the line fit to them are the cumulative bubble size distributions indicated by log ($N > V$) ~ log N, both are normalized to melt volume, not the bulk volume (bubble + melt) (Figure reproduced from Bai et al., 2010, *Journal of Geophysical Research* by permission of the American Geophysical Union).

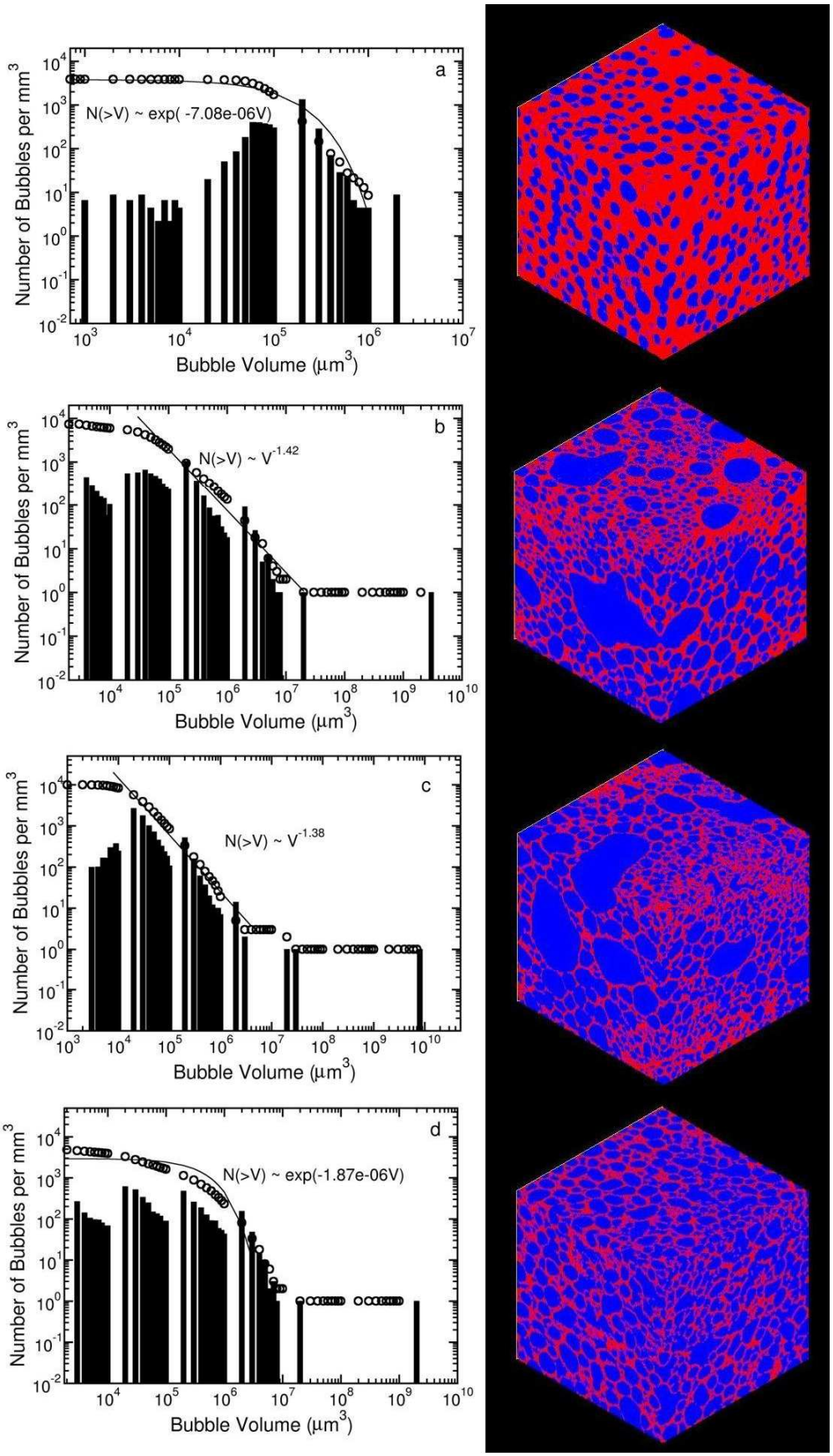
a
N(>V) ~ exp(-7.08e-06V)
Number of Bubbles per mm3
Bubble Volume (µm3)
b
N(>V) ~ V-1.42
Number of Bubbles per mm3
Bubble Volume (µm3)
c
N(>V) ~ V-1.38
Number of Bubbles per mm3
Bubble Volume (µm3)
d
N(>V) ~ exp(-1.87e-06V)
Number of Bubbles per mm3
Bubble Volume (µm3)

Figure 5.2 Permeability constants k_1 and k_2 and porosity-pore size relationships from measurements (**a, b**), and the relation between the geometry factor of α and the bubble diameter D (μm) (**c**). See text for a complete discussion (Figure reproduced from Bai et al., 2010, *Journal of Geophysical Research* by permission of the American Geophysical Union).

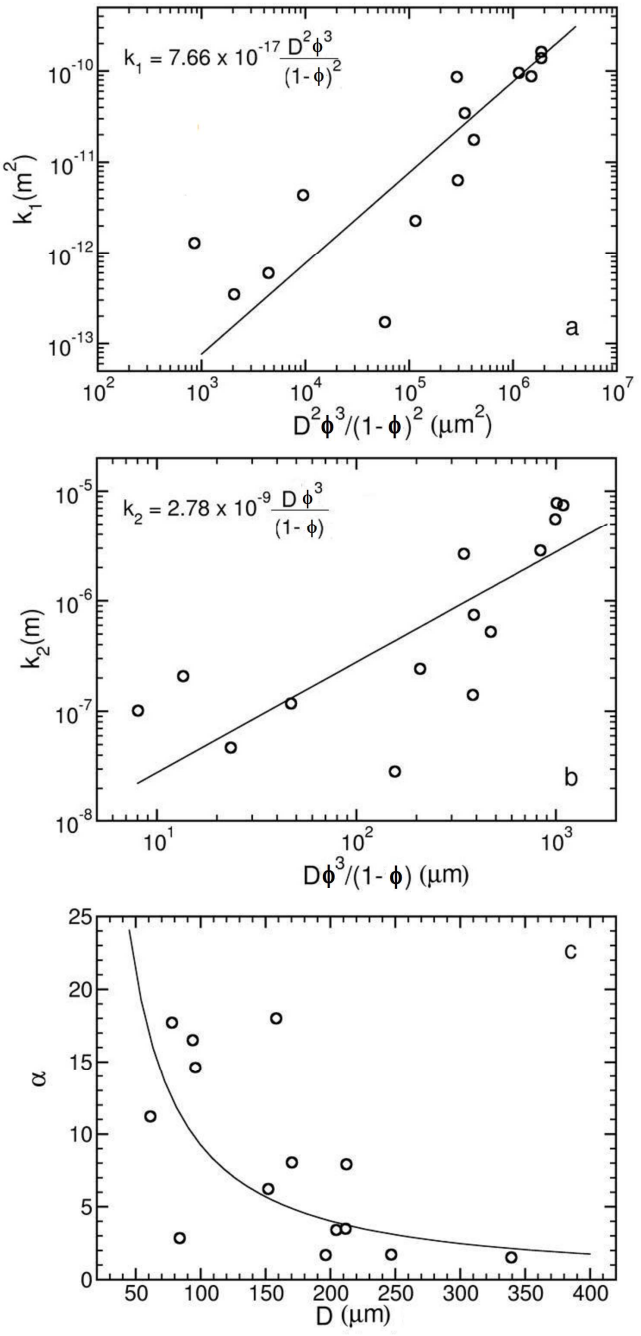

Figure 5.3 Relationship between the friction factor, f_k, and the Forchheimer number, *Fo*, for experimental measurements (**a**) and for lattice-Boltzmann simulations (**b**) from samples with different porosities. The uncertainties are shown in the results of fitting: $f_k = (1.11 \pm 0.17) + \frac{0.66 \pm 0.39}{Fo}$ (measurements) and $f_k = (0.59 \pm 0.49) + \frac{1.0 \pm 0.01}{Fo}$ (LB simulations) (Figure reproduced from Bai et al., 2010, *Journal of Geophysical Research* by permission of the American Geophysical Union).

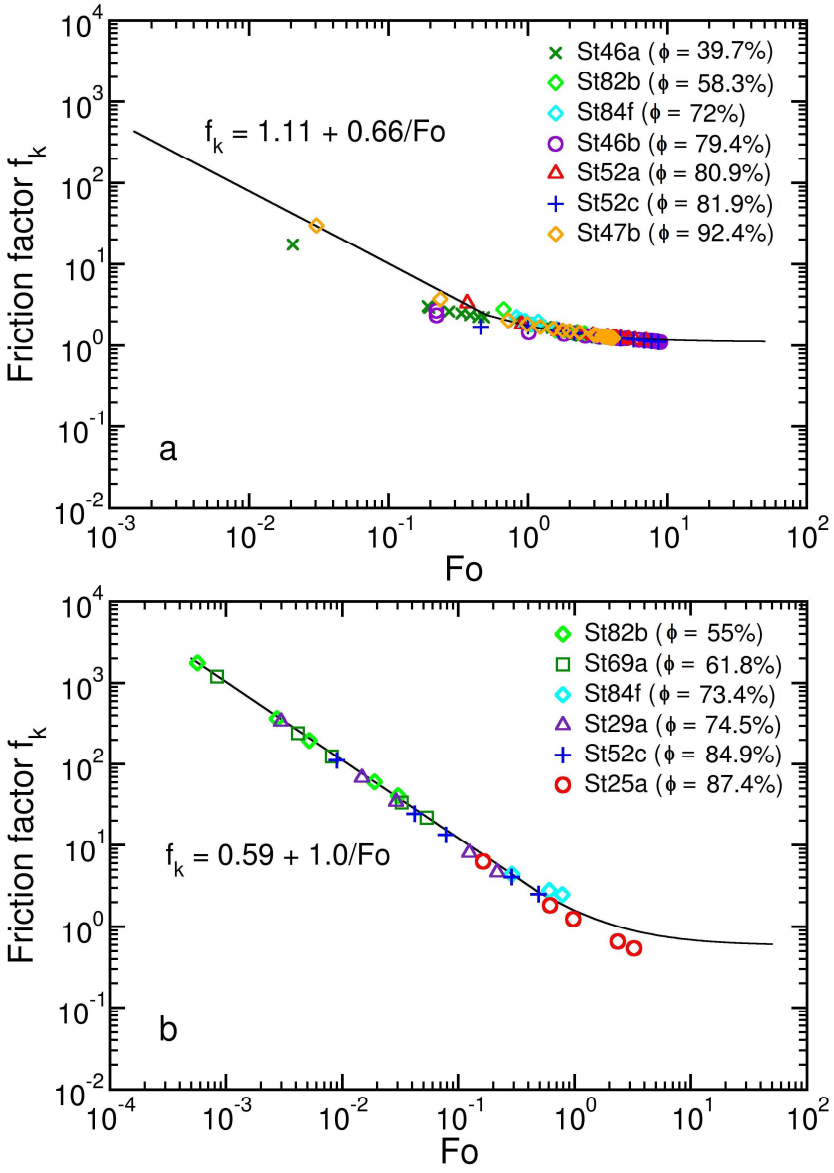

Figure 5.4 Permeability, *k*, and total porosity, ϕ, relationships from lattice-Boltzmann simulations and measurements in crystal-bearing samples. The permeability results of crystal-free samples are from section 4.1. The uncertainty in crystal-free samples (black symbols) is indicated by the error bars shown in Figure 4.1a. The uncertainties in permeabilities from LB simulations are given by the standard deviations (see Table 4.2) (Figure reproduced from Bai et al., 2011, *Geophysical Research Letters* by permission of the American Geophysical Union).

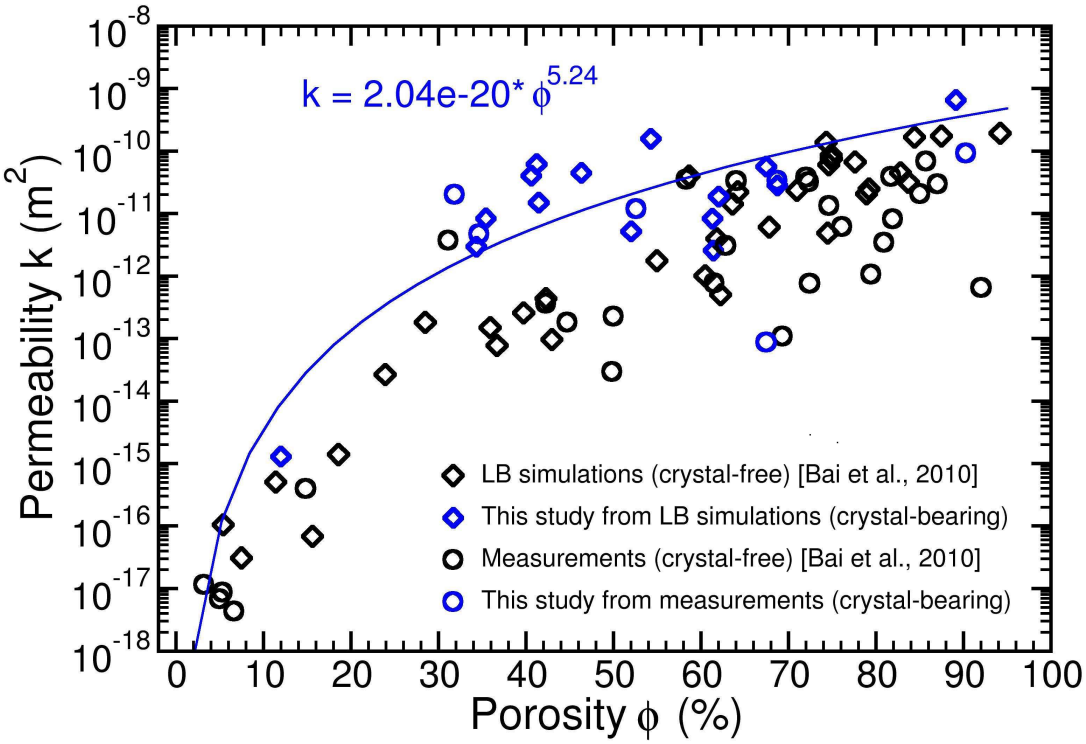

CHAPTER 6: IMPLICATIONS FOR STOMBOLI BASALT VOLCANO

6.1 Implications for Darcian to non-Darcian flow transitions

One of the significant trends in our permeability-porosity relationships is revealed in the transition from high pressure, low porosity, to low pressure (1 bar), high porosity degassing. The permeability is low (10^{-17} to 10^{-14} m^2) at porosities below ~ 29%, corresponding to small amounts of degassing expected at large depths; the permeability increases markedly in the porosity range ~ 18.5 to 29% as the percolation threshold is approached, and permeabilities finally attain values of 10^{-10} to 10^{-9} m^2 at porosities over ~ 65%.

We create a simple model to investigate the gas phase fraction exsolved from a magma and the permeability it creates during ascent. We consider the case of a basaltic magma consisting of a water-bearing melt and a gas phase composed only of H_2O (i.e., steam). Magmas with initial dissolved water concentrations of 1, 2, and 4% are modeled as they ascend to the surface, decompress, and exsolve water. In the model, the melt density remains constant at 2.6 kg/m^3, and the water within the volume of magma includes dissolved and exsolved H_2O (gas phase). The dissolved H_2O is determined by the H_2O solubility at each pressure (Dixon et al., 1995). Then we can calculate the total mass of exsolved of H_2O ($H_2O_{exsolved}$) for magmas with different initial concentrations of H_2O_{total} by:

$$H_2O_{exsolved} = H_2O_{total} - H_2O_{dissolved\ in\ melt} \quad (6.1)$$

We determine the water density at each pressure using equation of state of H_2O at high pressures and temperatures (Duan and Zhang, 2006), then we can calculate the volume fraction of exsolved H_2O (V_{H2O}%) during decompression by:

$$V_{H2O}\% = (H_2O_{exsolved}/\rho_{H2O})/(H_2O_{exsolved}/\rho_{H2O} + Melt_{basalt}/\rho_{basalt}) \quad (6.2)$$

The relation between pressure (bars) and volume fraction of H_2O is presented in Figure 6.1a. Considering the volume fraction of exsolved H_2O equivalent to the porosity of the magma, we calculate the permeability using the porosity-permeability relationship derived from our measurements of crystal free experiments and obtain a pressure-permeability relationship, or a depth-permeability relationship (Figure 6.1b). For a magma initially with 1 wt% H_2O, the significant increase in permeability occurs at depths of 10 to 200 m. For a basaltic magma containing about 2 to 3 wt% water, the significant increase of permeability begins to occur at a depth of 600 to 1100 m (~ 300 to 600 bar). This depth is very close to the depth below basaltic volcanoes where the permeable bubble network is proposed to occur (Jaupart and Vergniolle, 1989; Harris and Stevenson, 1997). The permeability increases at these depths are associated with bubble growth and coalescence, which produce permeable paths in the vesicular magma (Klug and Cashman, 1996); thus, gas may flow from coalesced bubbles through bubble apertures toward the surface of the Earth (Gonnermann and Manga, 2007). Our model shows that at the porosity of ~ 70 to 80% which is the magma fragmentation threshold value, the permeability can be in the order of ~ 10^{-12} m^2, this relatively low permeability might substantially increase the gas overpressure, causing magma fragmentation. Note that the fragmentation threshold values are mostly derived from measurements of porosity on natural samples, the pore size and porosity in these natural samples might be modified by posteruption processes (Vergniolle et al., 1996; Herd and Pinkerton, 1997; Thomas et al., 2004), therefore the fragmentation threshold might not be the critical porosity for the onset of magma fragmentation.

This and previous studies indicate that considerable inertial effects can be present when gas flows through a permeable magma under the conditions of magma degassing (Rust and Cashman, 2004; Takeuchi et al., 2008). We further examine the inertial effect based on the *Fo* value. Assuming a steam flow through a vesicular Stromboli basaltic magma with pores of 1 mm in diameter and a porosity 72%, we calculate the Forchheimer permeabilities, k_1 and k_2, of basaltic magma based on equations (5.2) and (5.3), giving $k_1 = 2.34 \times 10^{-10}$ m^2 and $k_2 = 4.79 \times 10^{-6}$ m. Assuming steam flow through this magma at 1200

ºC and 25 MPa (~ 1 km in depth), this density is 35.716 kg/m^3 and viscosity is 3.7037 × 10^{-5} Pa s. For a gas with a velocity 0.1 to 1 m/s, the Forchheimer number *Fo* varies from ~ 0.5 to 47. This range is close to the *Fo* value corresponding to the transition from Darcian to non-Darcian flow, implying that inertial effects play an important role under these eruption conditions. However, if at 1200 ºC and 25 MPa, a gas with a velocity of 10 m/s flows through the porous magma with a pore size over 5 mm, which has been observed in some basaltic systems (Harris and Stevenson, 1997), the calculated *Fo* can attain values as high as 912, far above the *Fo* value corresponding to the transition flow regimes. In this case, it is likely that a fully turbulent flow occurs in the vesicular magma. In Stromboli basaltic magma, large vesicles with sizes over 5 mm are commonly observed in scoria associated with the ordinary explosive activity (Polacci et al., 2008). During the ordinary explosive eruptions, the gas velocity can be over 10 m/s, in which case the turbulent gas flow is expected to occur in the vesicular Stromboli basaltic magma.

This turbulent gas flow in the porous magma is different from the gas slug flow or turbulent annular flow observed in paroxysmal Strombolian eruptions or Hawaiian eruptions (Vergniolle and Jaupart, 1986; Jaupart and Vergniolle, 1989; Seyfried and Freundt, 2000). In the gas slug regime, gas bubbles almost fill the entire diameter of volcanic conduit, and can collapse to turbulent annular flow upon bursting at the surface (Vergniolle and Jaupart, 1986; Seyfried and Freundt, 2000). However, below the conduit depth where the gas slug regime occurs, gas flows through the porous magma, and further studies on the connection between turbulent gas flow through the porous magma and gas slug flow need to be performed.

6.2 Implications for magma convection in Stromboli volcano conduit

Our studies show that crystals can increase permeability by 1–2 orders of magnitude at porosities of 31.6–55.3%. Crystal-bearing samples can produce extremely high *BNDs* that decrease significantly to lower values with increasing bubble growth durations. This implies that normal Strombolian eruptions are driven by crystal-rich and high *BND*

magmas. The higher permeability of the crystal-rich magma at shallow depths induces more-efficient gas loss during normal Stromboli eruptions and passive degassing, which results in a vesicle-poor, crystal-rich, dense magma after degassing, as shown from sample Str240506a and other studies (Lautze and Houghton, 2007; Polacci et al., 2008).

The densities and viscosities are 2500 and 2700 kg/m^3 and 15 to 20 versus 1.4×10^4 Pa s for LP and HP magmas, respectively (Métrich et al., 2001). The density contrast allows the HP magma to descend and cause mixing between the two magmas, as shown by Sr isotope variations (Francalanci et al., 1999, 2005) and crystal zoning (Landi et al., 2004). We estimate the crystal sinking velocity, U_c, by Stokes law: $U_c = \frac{2\Delta\rho_{c-l} g r_{cry}^2}{9\mu_{\mathrm{d}}}$, where μ_d, the viscosity of degassed HP magma, is 1.4×10^4 Pa s, r_{cry} is the crystal radius, and $\Delta\rho_{c-l}$, the density difference between the crystal and liquid, is 200 kg/m^3; g is gravitational acceleration. From X-ray μCT, most crystals in scoria are 0.16 to 0.3 mm in radius, and the calculated U_c is low (8×10^{-10} to 2.8×10^{-9} m/s), implying that most crystals are sinking together with the melt, not separately. Thus, we propose that the high-density, non-erupted, degassed HP magma can sit above the low density, volatile-rich LP magma, that eventually causes the paroxysmal explosions.

Analogue experimental studies on the mixing of the stratified liquids show that a low-density, low-viscosity liquid rises through a more dense, viscous overlying liquid (Huppert et al., 1986; Thomas et al., 1993). When the viscosity ratio between the two liquids is >300, the low-density, low-viscosity liquid flows up in a concentric pipe, and the high-density, high-viscosity one flows down at the periphery (Stevenson and Blake, 1998). According to Métrich et al. (2001), the viscosity ratio between HP and LP magmas is ~ 7000, therefore a similar flow pattern can be expected at Stromboli. Below the fragmentation level, magma flow can be described by Poiseuille flow (Kazahaya et al., 1994):

$$Q_{up} = \frac{\pi\Delta\rho_{l-l} g r_a^4}{8\mu_{\mathrm{a}}} \qquad (6.3)$$

$$Q_{down} = \frac{\pi \Delta \rho_{l-l} g}{8\mu_{\mathrm{d}}}[r_c^4 - r_a^4 - \frac{(r_c^2 - r_a^2)^2}{\ln(r_c / r_a)}] \quad (6.4)$$

where Q_{up} and Q_{down} are volume flux of ascending and descending magma respectively, $\Delta\rho_{l-l}$ is the density difference between the two magmas, r_a and r_c are the radius of the central ascending magma flow and volcano conduit radius, μ_a, and μ_d are the viscosities of the ascending and descending magmas, respectively. The 2003 paroxysmal eruption produced a mass discharge rate of 2.8 to 3.6×10^6 kg/s (Rosi et al., 2006). The fraction of juvenile material erupted was 0.81. If we consider that the juvenile materials are from the ascending LP magma that has a density of 1200 kg/m^3 (melt + gas), then $\Delta\rho_{l-l}$ =1500 kg/m^3; the calculated ascending magma volume flux is 1893 to 2434 m^3/s, and the calculated descending magma volume flux is 1922 to 1983 m^3/s for a conduit radius r_c of 10 m, and 19 to 21 m^3/s for a conduit radius r_c of 4 m. Our calculations show that the LP magma flowing up the center of a pipe might efficiently transfer LP magma to the overlying HP viscous magma for a volcano conduit radius between 4 to 10 m, which is the accepted value for the Stromboli volcano conduit (Stevenson and Blake, 1998). Paroxysmal explosions are suggested to be generated by a batch of LP magma rising quickly through the shallow conduit (Métrich et al., 2005). Analogue experiments show that bubbles might form plumes or large pockets of coalesced bubbles because of the high viscosity of the upper liquid, such plumes or gas pockets efficiently transfer exsolved gas from the low-density, low viscosity liquid to overlying viscous liquid (Thomas et al., 1993). Thus, we propose that LP magma might be transferred through the high density, viscous HP magma and undergo rapid decompression causing paroxysmal explosions.

Figure 6.1 Relationship between volume fraction of H_2O and pressure (**a**) and permeability and depth (**b**). Solid symbols in Figure b represent the volume fraction H_2O above the percolation threshold (Figure reproduced from Bai et al., 2010, *Journal of Geophysical Research* by permission of the American Geophysical Union).

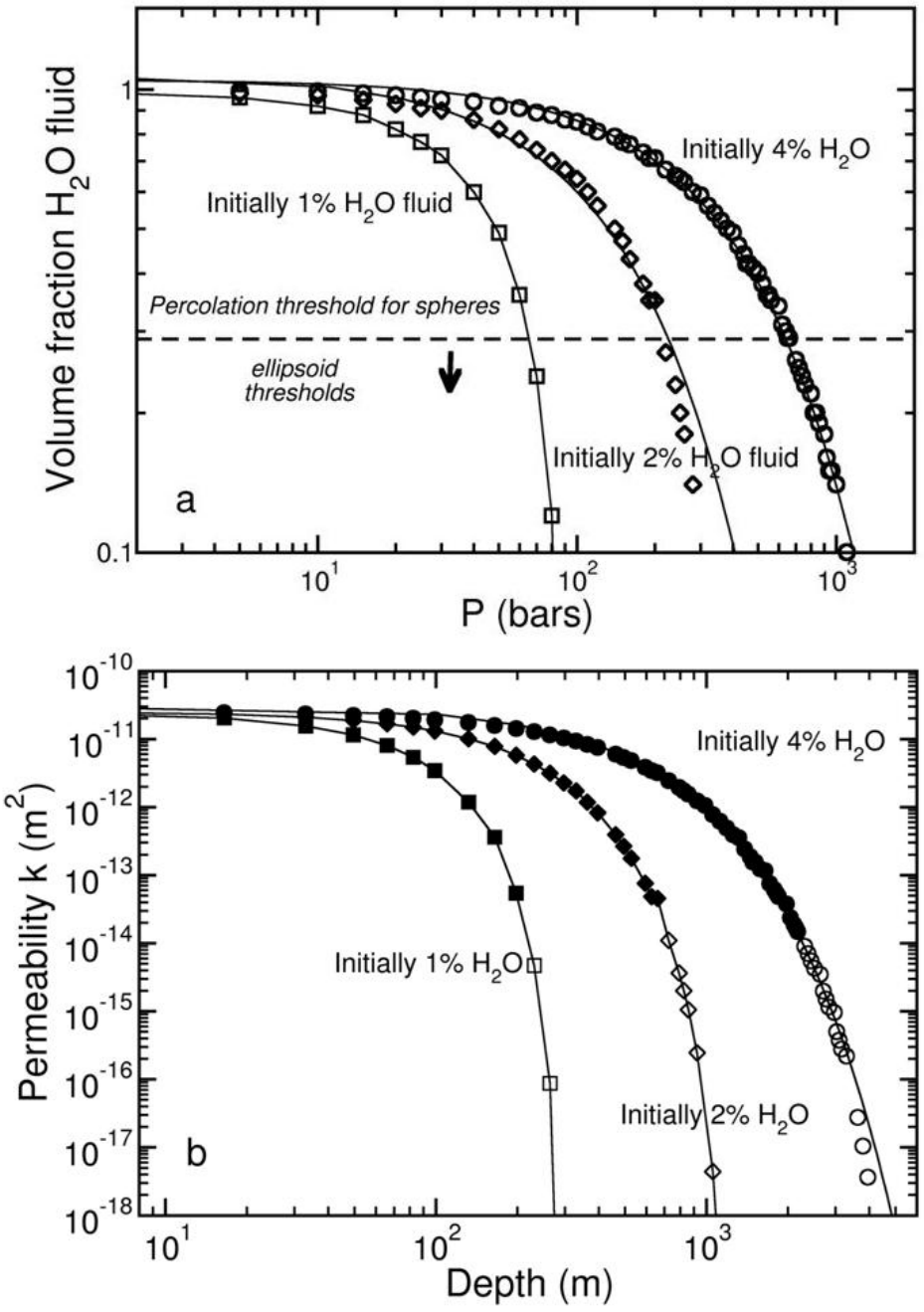

CHAPTER 7: CONCLUSIONS

This work compares bubble formation and growth, bubble sizes and distributions, and permeability development with porosity in crystal-free and crystal-bearing Stromboli basalts. The results can be used to constrain the dynamics of Stromboli volcano eruptions.

Lattice-Boltzmann simulations indicate that calculated permeabilities are strongly dependent on the simulation sample size at porosities less than ~ 65%, and that lattice-Boltzmann simulations generally produce higher permeabilities for small sample sizes ($N_L a$ < 714 to 761.6 μm). However, the permeability is insensitive to the simulation sample size in this study when porosities are greater than ~ 65%. The simulated permeability is not affected by the grid resolution variations over the range investigated.

The permeability and porosity in crystal-free Stromboli basaltic magma can be expressed by a power-law relationship: $k(\phi) = c\ (\phi)^5$, where $c = 2.35 \times 10^{-20}$ (LB simulations) and $c = 5.33 \times 10^{-21}$ (measurements). The permeability and porosity in crystal-bearing Stromboli basaltic magma can also be expressed by a power-law relationship: $k(\phi) = c\ (\phi)^{5.24}$, where $c = 2.04 \times 10^{-20}$ (LB simulations). Bubble sizes and distributions affect the Darcian permeability k_1 and non-Darcian permeability k_2. Variations in k_1 and k_2 with porosity ϕ and bubble diameter D are fit well to the Ergun relation, with $k_1 = 7.66\times10^{-17}\frac{D^2\phi^3}{(1-\phi)^2}$ and $k_2 = 2.78\times10^{-9}\frac{D\phi^3}{1-\phi}$. Our results show that at porosities above the sphere percolation threshold, ~ 29 volume percent, permeabilities are 1 to 2 orders of magnitude higher than in rhyolitic and dacitic volcanic rocks; the high permeabilities in these basaltic foams are attributed to a higher bubble interconnectivity and large bubble apertures due to bubble coalescence in these low viscosity melts.

Both simulations and measurements show that two regimes of flow occur in vesicular basaltic porous media. One is the Darcian flow regime (Fo < ~ 0.2 to 1) and the other is a transitional flow regime (1< Fo < 1 to 10). In this second regime, inertial forces begin to

dominate over viscous forces. The friction factor f_k derived from the Forchheimer equations is strongly dependent on k_2, the pore size, and the pore geometry factor at large *Fo*. The correlations between f_k and *Fo* from measurements agree well with those from simulations, where $f_k = (1.11 \pm 0.17) + \frac{0.66 \pm 0.39}{Fo}$ (measurements) and $f_k = (0.59 \pm 0.49) + \frac{1.0 \pm 0.01}{Fo}$ (LB simulations). The variations between f_k and *Fo* indicate a gradual change from Darcian to non-Darcian flow, rather than an abrupt change.

Our study also demonstrates that the permeabilities of crystal-bearing Stromboli basaltic magmas are about 1–2 orders of magnitude higher than those in aphyric magmas at porosities of 31.6 to 55.3%. We propose that efficient degassing pathways in the crystal-rich, scoria-producing, shallow Stromboli magma results in a degassed magma that sits above the crystal-poor, volatile-rich LP magma and would descend, the LP magma flows up in the concentric pipe due to large viscosity differences. Our magma flux calculations indicate that this type of convection can efficiently transfer LP magma and exsolved gas through the overlying degassed HP magma, potentially resulting in a more-violent paroxysmal explosion.

Modelling the depth-permeability relationship for magmas with initial concentrations of H_2O from 1 to 4 wt% indicate that high permeability magmas can occur at depths of ~ 100 to 2000 m (~ 3 to 600 bar). A gas flow at velocities of 0.1 to 1 m/s through pore sizes of ~ 1 mm is in the transition flow regime, and the inertial effects should be considered in modelling degassing at these depths. For a gas flow with a velocity over 10 m/s through porous Stromboli magma with a vesicle size over ~ 5 mm, *Fo* can attain values well above the transition, implying that inertia dominant, non-Darcian flow or turbulent flow probably prevails in the vesicular magma.

However, in our experimental studies, we did not investigate the effect of other volatiles such as CO_2, S, and Cl on the Stromboli basalt degassing. These volatiles comprise a large portion of the volatile budget in the Stromboli magma system (Métrich

et al., 2001; Bertaginini et al., 2003; Burton et al., 2007). Future degassing experiments should be performed with these dissolved volatiles. Also, we did not address the effect of crystallization, and magma mixing on convection between these two magmas. Future work should incorporate crystallization and magma mixing on the convection model, then the oscillation frequency might be more closely matched to the real oscillation frequency of Stromboli eruptions.

References

Aiuppa A, Moretti R, Federico C, Giudice G, Gurrieri S, Liuzzo M, Papale P, Shinohara H, Valenza M, Forecasting Etna eruptions by real-time observation of volcanic gas composition, *Geology*, 2007, 35: 1115–1118, doi:10.1130/G24149A.1

Aiuppa A, Burton M, Caltabiano T, Giudice G, Guerrieri S, Liuzzo M, Murè F, Salerno G, Unusually large magmatic CO_2 gas emissions prior to a basaltic paroxysm, *Geophys. Res. Lett.*, 2010, 37, L17303, doi:10.1029/2010GL043837

Allard P, A CO_2-rich gas trigger of explosive paroxysms at Stromboli basaltic volcano, Italy, *J. Volcanol. Geotherm. Res.*, 2010, 189: 363–374, doi:10.1016/j.jvolgeores.2009.11.018

Andrade J S, Costa U M S, Almeida M P, Makse H A, Stanley H E, Inertial effects on fluid flow through disordered porous media, *Phys. Rev. Lett.*, 1999, 82: 5249–5252, doi:10.1103/PhysRevLett.82.5249

Armienti P, Francalanci L, Landi P, Textural effects of steady state behaviour of the Stromboli feeding system, *J. Volcanol. Geotherm. Res.*, 2007, 160: 86–98, doi:10.1016/j.jvolgeores.2006.05.004

Arns C H, Knackstedt M A, Martys N S, Cross-property correlations and permeability estimation in sandstone, *Phys. Rev. E*, 2005, 72, 046304, doi:10.1103/PhysRevE.72.046304

Bai, L-P, Baker D R, Rivers M, Experimental study of bubble growth in Stromboli basalt melts at 1 atm, *Earth Planet. Sci. Lett.*, 2008, 267: 533–567, doi:10.1016/j.epsl.2007.11.063

Barberi F, Rosi M, Sodi A, Volcanic hazard assessment at Stromboli based on review of historical data, *Acta Vulcanolo.*, 1993, 3: 173–187

Belien I B, Cashman K V, Rempel A W, Gas accumulation in particle-rich suspensions and implications for bubble populations in crystal-rich magma, *Earth Planet. Sci. Lett.*, 2010, 297: 133–140, doi:10.1016/j.epsl.2010.06.014

Benson P M, Thompson B D, Meredith P G, Vinciguerra S, Young R P, Imaging flow failure in triaxially deformed Etna basalt using 3D acoustic-emission location and X-ray computed tomography, *Geophys. Res. Lett.*, 2007, 34, L03303, doi:10.1029/2006GL028721

Bertagnini A, Coltelli M, Landi P, Pompilio M, Rosi M, Violent explosions yield new insight into dynamics of Stromboli volcano, *Eos Trans*. *AGU*, 1999, 80(52): 633-636, doi:10.1029/99EO00415

Bertagnini A, Métrich N, Landi P, Rosi M, Stromboli volcano (Aeolian Archipelago Italy): An open window on the deep-feeding system of a steady state basaltic volcano, *J*. *Geophys*. *Res*., 2003, 108 (B7), 2336, doi:1029/2002JB002146

Blower J D, Factors controlling permeability-porosity relationships in magma, *Bull*. *Volcanol*., 2001, 63: 497–504, doi:10.1007/s004450100172

Blower J D, Keating J P, Mader H M, Phillips J C, Inferring volcanic degassing processes from vesicle size distributions, *Geophys*. *Res*. *Lett*., 2001, 28: 347–350, doi:10.1029/2000GL012188

Bosl W J, Dvorkin J, Nur A, A study of porosity and permeability using a lattice Boltzmann simulation, *Geophys*. *Res*. *Lett*., 1998, 25(9): 1475–1478, doi:10.1029/98GL00859

Brinkman H C, A calculation of the viscous force exerted by a flowing fluid on a dense swarm of particles, *Appl*. *Sci*. *Res*., 1947, 27–34, doi:10.1007/BF02120313

Burgisser A, Gardner J E, Experimental constrains on degassing and permeability in volcanic conduit flow, *Bull*. *Volcanol*., 2005, 67: 42–56, doi:10.1007/s00445-004-0359-5

Burton M R, Mader H M, Polacci M, The role of gas percolation in quiescent degassing of persistently active basaltic volcanoes, *Earth Planet*. *Sci*. *Lett*., 2007, 264: 46–60, doi:10.1016/j.epsl.2007.08.028

Cluzel N, Laporte D, Provost A, Kannewischer I, Kinetics of heterogeneous bubble nucleation in rhyolitic melts: Implications for the number density of bubbles in volcanic conduits and for pumice textures, *Contrib*. *Mineral Petrol*., 2008, 156: 745–763, doi:10.1007/s00410-008-0313-1

Collombet M, Two-dimensional gas loss for silicic magma flows: Toward more realistic numerical models, *Geophy*. *J*. *Int*., 2009, 177: 309–318, doi:10.1111/j.1365-246X.2008.04086.x

Consiglio R, Baker D R, Paul G, Stanley H E, Continuum percolation thresholds for mixtures of spheres of different sizes, *Physica A*, 2003, 319: 49–55, doi:10.1016/S0378-4371(02)01501-7

Dixon J E, Stolper E M, Holloway J R, An experimental study of water and carbon dioxide solubilities in mid-ocean ridge basaltic liquids. Part I: calibration and solubility, *J. Petrology*, 1995, 36(6): 1607–1631

Duan Z, Zhang Z, Equation of state of the H_2O, CO_2 and H_2O-CO_2 systems up to 10 GPa and 2573.15 K: Molecular dynamics simulations with ab initio potential surface, *Geochim. Cosmochim. Acta*, 2006, 70: 2311–2324, doi:10.1016/j.gca.2006.02.009

Dybbs A, Edwards R V, A new look at porous media fluid mechanics-Darcy to turbulent, in *Fundamentals of Transport Phenomena in Porous Media*, edited by J Bear and M Y Corapcioglu, Martinus Nijhoff, Dordrecht, 1984, pp: 199–256

Eichelberger J C, Carrigan C R, Westrich H R, Price R H, Non-explosive silicic volcanism, *Nature*, 1986, 323: 598–602, doi:10.1038/323598a0

Ergun S, Fluid through packed columns, *Chem. Eng. Prog.*, 1952, 48: 89–94

Francalanci L, Tommasini S, Conticelli S, Davies G R, Sr isotope evidence for short magma residence time for the 20th century activity at Stromboli volcano, Italy, *Earth Planet. Sci. Lett.*, 1999, 167: 61–69, doi:10.1016/S0012-821X(99)00013-8

Francalanci L, Tommasini S, Conticelli S, The volcanic activity of Stromboli in the 1906-1998 AD period: Mineralogical, geochemical and isotope data relevant to the understanding of the plumbing system, *J. Volcanol. Geotherm. Res.*, 2004, 131:179–211, doi:10.1016/S0377-0273(03)00362-7

Francalanci L, Davies G R, Lustenhouwer W, Tommasini S, Mason P R D, Conticelli S, Intra-grain Sr isotope evidence for crystal recycling and multiple magma reservoirs in the recent activity of Stromboli volcano, southern Italy, *J. Petro.*, 2005, 46: 1997–2021, doi:10.1093/petrology/egi045

Frank X, Dietrich N, Wu J, Barraud R, Li H-J, Bubble nucleation and growth in fluids, *Chem. Eng. Sci.*, 2007, 62: 7090–7097, doi:10.1016/j.ces.2007.08.030

Fredrich J T, DiGiovanni A A, Noble D R, Predicting macroscopic transport properties using microscopic image data, *J. Geophys. Res.*, 2006, 111, B03201, doi: 10.1029/2005JB003774

Gardner J, Hilton M, Carroll M, Experimental constraints on degassing of magma: Isothermal bubble growth during continuous decompression from high pressure, *Earth Planet. Sci. Lett.*, 1999, 168: 201–218, doi:10.1016/S0012-821X(99)00051-5

Gardner J E, Heterogeneous bubble nucleation in highly viscous silicate melts during instantaneous decompression from high press, *Chem. Geol.*, 2007, 236: 1–12, doi:10.1016/j.chemgeo.2006.08.006

Giordano D, Dingwell D B, Non-Arrhenian multicomponent melt viscosity: A model, *Earth Planet. Sci. Lett.*, 2003, 208: 337–349, doi:10.1016/S0012-821X(03)00042-6

Gonnermann H M, Manga M, The fluid mechanics inside a volcano, *Annu. Rev. Fluid Mech.*, 2007, 39: 321–356, doi:10.1146/annurev.fluid.39.050905.110207

Harris A J L, Stevenson D S, Magma budget and steady-state activity of Vulcano and Stromboli, *Geophys. Res. Lett.*, 1997, 24(9): 1043–1046, doi:10.1029/97GL00861

Harting J, Venturoli M, Coveney P V, Large-scale grid-enabled lattice-Boltzmann simulations of complex fluid flow in porous media and under shear, *Phil. Trans. R. Soc. London, Ser. A*, 2004, 362: 1703–1722, doi:10.1098/rsta.2004.1402

Herd R, Pinkerton H, Bubble coalescence in basaltic lava: Its impact on the evolution of bubble populations, *J. Volcanol. Geotherm. Res.*, 1997, 75: 137–157, doi:10.1016/S0377-0273(96)00039-X

Hill R J, Koch D L, Ladd A J C, The first effects of fluid inertia on flows in ordered and random arrays of spheres, *J. Fluid Mech.*, 2001, 448: 213–241, doi:10.1017/S0022112001005948

Hill R J, Koch D L, The transition from steady to weakly turbulent flow in a close-packed ordered array of spheres, *J. Fluid Mech.*, 2002, 465: 59–97, doi:10.1017/S0022112002008947

Holdich R G, Fluid flow in porous media, in *Fundamentals of particle technology*, Midland Information Technology and Publishing, UK, 2002, pp: 21–28

Huppert H E, Sparks R S J, Whitehead J A, Hallworth M A, Replenishment of magma chambers by light inputs, *J. Geophys. Res.*, 1986, 91: 6113–6122, doi:10.1029/JB091iB06p06113

Hurwitz S, Navon O, Bubble nucleation in rhyolitic melts: Experiments at high pressure, temperature, and water content, *Earth Planet. Sci. Lett.*, 1994, 122: 267–280, doi:10.1016/S0012-821X(94)90001-9

Innocentini M D M, Pardo A R F, Pandolfelli V C, Influence of air compressibility on the permeability evaluation of refractory castables, *J. Am. Ceram. Soc.*, 2000, 83: 1536–1538, doi:10.1111/j.1151-2916.2000.tb01426.x

Jaupart C, Vergniolle S, The generation and collapse of a foam layer at the roof of a basaltic magma chamber, *J. Fluid Mech.*, 1989, 203: 347–380, doi:10.1017/S0022112089001497

Jaupart C, Allègre C J, Gas content, eruption rate and instabilities of eruption regime in silicic volcanoes, *Earth Planet. Sci. Lett.*, 1991, 102: 413–429, doi:10.1016/0012-821X(91)90032-D

Kazahaya K, Shinohara H, Saito G, Excessive degassing of Izu-Oshima volcano: Magma convection in a conduit, *Bull. Volcanol.*, 1994, 56: 207–216, doi:10.1007/BF00279605

Keehm Y, Mukerji T, Nur A, Permeability predication from thin sections: 3D reconstruction and Lattice-Boltzmann flow simulation, *Geophy. Res. Lett.*, 2004, 31, L04606, doi:10.1029/2003GL018761

Ketcham R A, Three-dimensional grain fabric measurements using high-resolution X-ray computed tomography, *J. Struct. Geol.*, 2005, 27: 1217–1228, doi:10.1016/j.jsg.2005.02.006

Klug C, Cashman K V, Permeability development in vesiculating magmas: Implications for fragmentation, *Bull. Volcanol.*, 1996, 58: 87–100, doi:10.1007/s004450050128

Klug C, Cashman K V, Bacon C R, Structure and physical characteristics of pumice from the climatic eruption of Mount Mazama (Crater Lake), Oregon, *Bull. Volcanol.*, 2002, 64: 486–501, doi:10.1007/s00445-002-0230-5

Landi P, Métrich N, Bertagnini A, Rosi M, Dynamics of magma mixing and degassing recorded in plagioclase at Stromboli (Aeolian Aechipelago, Italy), *Contrib. Mineral. Petrol.*, 2004, 147: 213–227, doi:10.1007/s00410-004-0555-5

Landi P, Francalanci L, Pompilio M, Rosi M, Corsaro R A, Petrone C M, Nardini I, Miraglia L, The December 2002–July 2003 effusive event at at Stromboli volcano,

Italy: Insights into the shallow plumbing system by petrochemical studies, *J. Volcanol. Geotherm. Res.*, 2006, 155: 263–284, doi:10.1016/j.jvolgeores.2006.03.032

Larsen J F, Gardner J E, Experimental constraints on bubble interactions in rhyolite melts: Implications for vesicle size distributions, *Earth Planet. Sci. Lett.*, 2000, 180: 201–214, doi:10.1016/S0012-821X(00)00166-7

Larsen J F, Denis M H, Gardner J E**,** Experimental study of bubble coalescence in rhyolitic and phonolitic melts, *Geochi. Cosmochim. Acta*, 2004, 68: 333–344, doi:10.1016/S0016-7037(03)00412-5

Lautze N C, Houghton B F, Linking variable explosion style and magma textures during 2002 at Stromboli volcano, Italy, *Bull. Volcanol.*, 2007, 69: 445–460, doi:10.1007/s00445-006-0086-1

Lautze N C, Sisson T W, Mangan M T, Grove T L, Segregating gas from melt: An experimental study of the Ostwald ripening of vapor bubbles in magmas, *Contrib. Mineral. Petro.*, 2011, 161: 331–347, doi:10.1007/s00410-010-0535-x

Lofgren G, Experimental studies on the dynamic crystallization of silicate melts, in *Physics of Magmatic Processes*, edited by R B Hargraves, *Geol*ogy, 1980, *pp*: 487–551

Mangan M T, Sisson T W, Hankins W B, Decompression experiments identify kinetic controls on explosive silicic eruptions, *Geophys. Res. Lett.*, 2004, 31, L08605, doi:10.1029/2004GL019509

Manwart C, Aaltosalmi U, Koponen A, Hilfer R, Timonen J, Lattice-Boltzmann and finite-difference simulations for the permeability for three-dimensional porous media, *Phys. Rev. E*, 2002, 66, 016702, doi:10.1103/PhysRevE.66.016702

Martel C, Bureau H, In situ high-pressure and high-temperature bubble growth in silicic melts, *Earth Planet. Sci. Lett.*, 2001, 191, 115–127, doi:10.1016/S0012-821X(01)00407-1

Marti J, C Soriano, Dingwell D B, Tube pumices as strain markers of the ductile-brittle transition during magma fragmentation, *Nature*, 1999, 402: 650–653, doi:10.1038/45219

Martino S D, Palo M, Cimini G B, A statistical study of the Stromboli volcano explosion quakes before and during 2002-2003 eruptive crisis, *J. Geophys. Res*., 2011, 116, B04303, doi:1029/2010JB008047

Martys N S, Chen H, Simulation of multicomponent fluids in complex three-dimensional geometries by the lattice Boltzmann method, *Phys. Rev. E*, 1996, 53: 743–750, doi:10.1103/PhysRevE.53.743

Melnik O, Sparks R S J, Non-linear dynamics of lava dome extrusion, *Nature*, 1999, 402: 37–41, doi:10.1038/46950

Métrich N, Bertagnini A, Landi P, Rosi M, Crystallization driven by decompression and water loss at Stromboli (Aeolian Archipelago, Italy), *J. Petro*., 2001, 42: 1471–1490, doi:10.1093/petrology/42.8.1471

Métrich N, Bertagnini A, Landi P, Rosi M, Belhadj O, Triggering mechanism at the origin of paroxysms at Stromboli (Aeolian Archipelago, Italy): The 5 April 2003 eruption, *Geophys. Res. Lett*., 2005, 32, L10305, doi:10.1029/2004GL022257

Métrich N, Bertagnini A, Muro A D, Conditions of magma storage, degassing and ascent at Stromboli: New insight into the volcano plumbing system with inferences on the eruptive dynamics, *J. Petro*., 2010, 51: 603–626, doi:10.1093/petrology/egp083

Mueller S, Melnik O, Spieler O, Scheu B, Dingwell D B, Permeability and degassing of dome lavas undergoing rapid decompression: An experimental determination, *Bull. Volcanol*., 2005, 67: 526–538, doi:10.1007/s00445-004-0392-4

Navon O, Lyakhovsky V, Vesiculation processes in silicic magmas, in *The Physics of Explosive Volcanic Eruptions*, edited by J S Gilbert and R S Sparks, *Geol. Soc. Spec. Publ*., 1998, 145: 27–50

Okumura S, Nakamura M, Tsuchiyama A, Nakano T, Uesugi K, Evolution of bubble microstructure in sheared rhyolite: Formation of a channel-like bubble network, *J. Geophys. Res*., 2008, 113, B07208, doi:10.1029/2007JB005362

Polacci M, Baker D R, Mancini L, Tromba G, Zanini F, Three-dimensional investigation of volcanic textures by X-ray microtomography and implications for conduit processes, *Geophys. Res. Lett*., 2006, 33, L13312, doi:10.1029/2006GL026241

Polacci M, Baker D R, Bai L-P, Mancini L, Large vesicles record pathways of degassing at basaltic volcanoes, *Bull. Volcanol*., 2008, 70: 1023–1029, doi:10.1007/s00445-007-0184-8

Polacci M, Baker D R, Mancini L, Favretto S, Hill R J, Vesiculation in magmas from Stromboli and implications for normal Strombolian activity and paroxysmal explosions in basaltic systems, *J. Geophys. Res*., 2009, 114, B01206, doi: 10.1029/2008JB005672

Rasband W S, ImageJ, U. S. National Institutes of Health, Bethesda, Maryland, USA, 1997, http://rsb.info.nih.gov/ij/

Rintoul M D, Torquato S, Reconstruction of structure of dispersion, *J. Colloid Interface Sci*., 1997, 186: 467–476, doi:10.1006/jcis.1996.4675

Ripepe M, Harris A J L, Dynamics of the 5 April 2003 explosive paroxysm observed at Stromboli by a near-vent thermal, seismic and infrasonic array, *Geophys. Res. Lett*., 2008, 35, L07306, doi:10.1029/2007GL032533

Rosi M, Bertagnini A, Harris A J L, Pioli L, Pistolesi M, Ripepe M, A case history of paroxysmal explosion at Stromboli: Timing and dynamics of the April 5, 2003 event, *Earth Planet. Sci. Lett*., 2006, 243: 594–606, doi:10.1016/j.epsl.2006.01.035

Rust A C, Cashman K V, Permeability of vesicular silicic magma: Inertial and hysteresis effect, *Earth Planet. Sci. Lett*., 2004, 228: 93–107, doi:10.1016/j.epsl.2004.09.025

Ruth D, Ma H, On the derivation of the Forchheimer equation by means of the averaging theorem, *Transp. Porous Media*, 1992, 7: 255–264, doi:10.1007/BF01063962

Saar M O, Manga M, Permeability-porosity relationship in vesicular basalts, *Geophys. Res. Lett*., 1999, 26: 111–114, doi:10.1029/1998GL900256

Saar M O, Manga M, Continuum percolation for randomly oriented soft-core prisms, *Phys. Rev. E*, 2002, 65, 056131, doi:10.1103/PhysRevE.65.056131

Seyfried R, Freundt A, Experiments on conduit flow and eruption behavior of basaltic vocanic eruptions, *J. Geophys. Res*., 2000, 105: 23727–23740, doi:10.1029/2000JB900096

Sidiropoulou M G, Moutsopoulos K N, Tsihrintzis V A, Determination of Forchheimer equation coefficients *a* and *b*, *Hydrol. Process*., 2007, 21: 534–554, doi:10.1002/hyp.6264

Sparks R S J, The dynamics of bubble formation and growth in magmas: A review and analysis, *J. Volcanol. Geotherm. Res.*, 1978, 3: 1–37, doi:10.1016/0377-0273(78)90002-1

Stevenson D S, Blake S, Modelling the dynamics and thermodynamics of volcanic degassing, *Bull. Volcanol.*, 1998, *60*, 307–317, doi:10.1007/s004450050234

Takeuchi S, Nakashima S, Tomiya A, Permeability measurements of natural and experimental volcanic materials with a simple permeameter: Toward an understanding of magmatic degassing processes, *J. Volcanol. Geotherm. Res.*, 2008, doi:10.1016/j.jvolgeores.2008.05.010

Thomas N, Tait S, Koyaguchi T, Mixing of stratified liquids by the motion of gas bubbles: Application to magma mixing, *Earth Planet. Sci. Lett.*, 1993, 115: 161–175, doi:10.1016/0012-821X(93)90220-4

Thomas N, Jaupart C, Vergniolle S, On the vesicularity of pumice, *J. Geophys. Res.*, 1994, 99: 15633–15644, doi:10.1029/94JB00650

Venkataraman P, Rao P R M, Darcian, transitional and turbulent flow through porous media, *J. Hydr. Engrg.*, 1998, 124(8): 840–846, doi:10.1061/(ASCE)0733-9429(1998)124:8(840)

Vergniolle S, Jaupart C, Separated two-phase flow and basaltic eruptions, *J. Geophys. Res.*, 1986, 91: 12842–12860, doi: 10.1029/JB091iB12p12842

Vergniolle S, Jaupart C, Dynamics of degassing at Kilauea volcano, Hawaii, *J. Geophys. Res.*, 1990, 95: 2793–2809, doi:10.1029/JB095iB03p02793

Vergniolle S, Brandeis G, Mareschal J C, Strombolian explosions 2. Eruption dynamics determined from acoustic measurements, *J. Geophys. Res.*, 1996, 101(B9): 20449–20466, doi:10.1029/96JB01925

Walsh S D C, Saar M O, Magma yield stress and permeability: Insights from multiphase percolation theory, *J. Volcanol. Geotherm. Res.*, 2008, 177: 1011–1019, doi:10.1016/j.jvolgeores.2008.07.009

Wood B D, Inertial effects in dispersion in porous media, *Water Resour. Res.*, 2007, 43, W12S16, doi:10.1029/2006WR005790

Wright H M, Roberts J J, Cashman K V, Permeability of anisotropic tube pumice: Model calculations and measurements, *Geophys*. *Res*. *Lett*., 2006, 33, L17316, doi: 10.1029/2006GL027224

Wright H M, Cashman K V, Gottesfeld E H, Roberts J J, Pore structure of volcanic clasts: Measurements of permeability and electrical conductivity, *Earth Planet*. *Sci*. *Lett*., 2009, 280: 93–164, doi:10.1016/j.epsl.2009.01.023

Yokoyama T, Takeuchi S, Porosimetry of vesicular volcanic products by a water-expulsion method and the relationship of pore characteristics to permeability, *J*. *Geophys*. *Res*., 2009, 114, B02201, doi: 10.1029/2008JB005758